Theoretical studies of graphene and graphene-related materials involving carbon and silicon

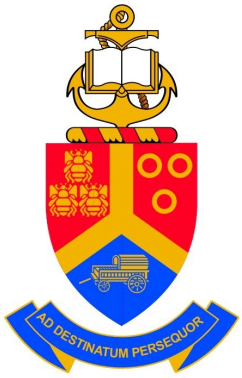

by
Refilwe Edwin Mapasha

Submitted in partial fulfilment of the requirements
for the degree
Magister Scientiæ
in the Faculty of Natural and Agricultural Sciences
University of Pretoria

Supervisor: Prof Nithaya Chetty

February 8, 2011

UNIVERSITEIT VAN PRETORIA
UNIVERSITY OF PRETORIA
YUNIBESITHI YA PRETORIA

UNIVERSITEIT VAN PRETORIA
UNIVERSITY OF PRETORIA
YUNIBESITHI YA PRETORIA

UNIVERSITY OF PRETORIA

DECLARATION OF ORIGINALITY

This document must be signed and submitted with every essay, report, project, assignment, dissertation and/or thesis.

Full names of student: Refilwe Edwin Mapasha

Student number: s29685712

Declaration

1. I understand what plagiarism is and am aware of the University's policy in this regard.
2. I declare that this dissertation is my own original work. Where other people's work has been used (either from a printed source, Internet or any other source), this has been properly acknowledged and referenced in accordance with departmental requirements.
3. I have not used work previously produced by another student or any other person to hand in as my own.
4. I have not allowed, and will not allow, anyone to copy my work with the intention of passing it off as his or her own.

SIGNATURE STUDENT:.....

SIGNATURE SUPERVISOR:.....

Theoretical studies of graphene and graphene-related materials involving silicon and carbon

by

Refilwe Edwin Mapasha

Supervised by Prof Nithaya Chetty

Faculty of Natural and Agricultural Sciences

Submitted in partial fulfilment of the requirements

for the degree Magister Scientiæ

Abstract

The structural and electronic properties of graphene and graphene-related materials have been intensively investigated using the plane wave based periodic density functional theory (DFT). The Vienna *ab initio* simulation package (VASP) code employing the generalized gradient approximation (GGA) for the exchange correlation potential was used. In all calculations, the geometry optimization option was employed in allowing the structure to fully relax.

Hydrogen adatoms were adsorbed on C, Si and SiC in the graphene structure involving (1x1),(2x2),(3x3) and (4x4) two dimensional unit cells. The density of states reveals that the adsorption of 50% hydrogen makes the system metallic but 100% coverage at the on top sites generates a band gap. Our results show that SiC in the graphene structure is a plausible structure with a wide band gap.

For adsoption of lithium adatoms, we considered various configurations involving the (1x1), (2x1) and (2x2) two-dimensional unit cells, and we consider the isolated Li dimer on graphene. We consider more detailed configurations than have been studied

before, and our results compare favourably with previously calculated results where such results exist.

For 100% coverage, we have new results for Li on the on-top site, which suggests a staggered configuration for the lowest energy structure for which the Li adatoms are alternately pushed into and pulled out of the graphene layer. For 50% coverage, Li favours the hollow site. We discovered that a careful relaxation of the system also shows a staggered configuration, a result that has not been investigated before.

Dedication

This is dedicated to the whole family of Balaudzi and to my late grandmother Mankwana. To my mom (Dorah) and dad (Mulambilu), this is for the love and support you have given me for the years of my studies.

Acknowledgements

I would like to acknowledge my supervisor Prof Nithaya Chetty for initiating this project, unfailing support, guidance, discussion and encouragement throughout this project. I would like to acknowledge Prof Johan Malherbe for financial support. I am extremely grateful to the National Institute of Theoretical Physics (NIThep) for financial assistance.

I would like to thank all members of the computational solid state research group at the University of Pretoria for support, and particularly Mr Richard Andrew for help with Latex.

I would like to thank all the family of Balaudzi ba Mapato a Senaba, especially my uncle Mohleiwana Mapasha for his academic and moral support throughout my studies. In particular, many thanks to my parents Dorah and Mulambilu Mapasha for their financial support and patience throughout my studies.

Contents

List of Figures

List of Tables

1

Introduction

Quantum mechanical modelling is the most accurate computational method used in calculating the energies and predicting the equilibrium structures of solid state and molecular systems. Such modelling provides quantitative predictions for a broad range of systems and is not limited to any type of materials. This gives us the assurance that by solving the quantum mechanical equations of a system, we can achieve a greater understanding of a large number of physical phenomena related to the properties of real material systems.

In this work, quantum mechanical modelling enables us to understand the electronic structure of graphene and to predict some of the not-as-yet experimentally discovered structures related to graphene. We employed density functional theory (DFT) methods to determine the energies of the systems. Our results are comparable with experiment where such results exist, which shows the accuracy of the DFT method.

The calculated energies enables us to find the equilibrium lattice constant by plotting the energies versus cell volumes which we fit to the Birch-Murnaghan equation of state. The energies were obtained by running several calculations at different vol-

umes. For the graphene structure, we plotted the energies versus lattice constants. The equilibrium lattice constant value coincides with the minimum total energy of the graphene. This is a well established method for accurately predicting the equilibrium lattice constants, bulk moduli, cohesive energies and transition pressures of the systems [33, 93].

We employ methods that replaces the chemically inert core electrons with pseudopotentials. Commonly used pseudopotentials are the norm conserving [109] pseudopotential followed by the ultrasoft pseudopotential [53]. Nowadays, the most popular is the projector-augmented wave (PAW) method introduced by Blochl [19]. In this project, the self consistent density functional theory is applied, using the generalized gradient approximation for the exchange and correlation potential to study the electronic structure of our systems. This enables us to accurately classify whether the system is metallic, insulator or semimetallic by computing the band structures and densities of states (DOS).

Our work is centred on altering the electronic structure of graphene using various adatoms. Hydrogen is the most obvious choice of dopant, and hydrogenated graphene, which is more commonly referred to as graphane[76, 95], has been studied very extensively[38]. The main results for our purposes are two fold: firstly, the energetically most favoured site for a single isolated hydrogen adatom on graphene is the on-top site and, secondly, 100% coverage at the on-top sites results in insulating behaviour, with the lowest energy configuration corresponding to hydrogen adatoms attaching alternately above and below the graphene layer. Simple electron counting arguments suggest that all the dangling bond states are saturated in this case which results in insulating behaviour. Electronic structure calculations of this system yield a relatively large band-gap in the region of $3.5eV$[104]for this material.

Li on graphene has also been studied previously by several authors[27, 65, 30], and here we extend this study to newer configurations. We furnish more detailed structural and electronic results. In our computations, we consider Li at the on-top site. For 100% coverage for Li on the on-top sites, we find results that are opposite to those of hydrogen on graphene. We establish that Li attaching on the same side of the graphene sheet is lower in energy compared with Li attaching alternately on opposite sides of the graphene sheet. We have calculated the detailed staggering of the Li adatoms in this case. The most favoured site for a single isolated Li adatom on graphene is the hollow site. This means that the maximum coverage that is attainable for Li at the hollow sites is only 50%. This results in an under-saturation of the dangling bond states and this gives rise to metallic behaviour. Our detailed relaxations show that the Li adatoms are staggered on the graphene layer.

For different coverages we have different ground state configurations. Our work shows that for 100% coverage on the on-top site, the ground state corresponds to Li attaching on the same side in a staggered configuration. For 50% coverage, we have demonstrated that the hollow site is favoured over the on-top site. The ground state configuration for this coverage corresponds to Li attaching on the same side in a staggered configuration. For even lower coverages, the hollow site is deemed to be more favourable. However, for very low coverages, the attachment on the same side or on opposite sides of the graphene sheet becomes degenerate.

1.1 Problem statement

Graphene, a single layer of graphite, has stimulated enormous scientific interest. The interest in graphene is primarily due to its unique (unusual) properties. It was discov-

ered that graphene has high electronic mobility and high charge carrier concentrations which makes graphene an interesting candidate for applications in electronic devices especially nano-scaled devices. The graphene structure is easily accessible and it is cheap to make.

Its many unique properties are still not properly understood, and need further investigations. Computer modelling in the past few years has contributed to the understanding of graphene. There is still more effort needed to understand the unique properties of this material. Hopefully, if such challenges are resolved, graphene will find more applications in nanotechnology.

1.2 Aims and objectives

The main aim of this project is to investigate graphene and graphene-related materials, involving Si and C. All calculations have been performed using the Vienna *ab initio* simulation package (VASP) code within the framework of density functional theory. Our work focuses on the following: firstly bulk carbon, bulk silicon in the diamond structure and silicon carbide in the zinc blende structure, followed by carbon, silicon and silicon carbide (SiC) in the graphene structure. We adsorb hydrogen as well as lithium adatoms on the graphene structures involving different supercell sizes. Our aim is to determine the structural and electronic properties of these different systems. Adsorption is used to generate and control the band gaps of the materials. To validate our work, our calculated results are compared with experimental results and other theoretical results obtained previously. The objectives of this study are the following:

1. To find the kinetics energy cutoffs for the plane wave expansion of the wavefunctions.

2. Determine the k-points sampling for the Brillouin zone of the systems.

3. Determine the structural properties of the systems such as the equilibrium lattice constant, volume and bond lengths.

4. Determine the bulk moduli of cubic systems.

5. Determine the electronic properties of the systems, i.e. density of states, band structures and charge densities that give an indication of the nature and bonding type of the systems.

1.3 Outline of the dissertation

This dissertation is divided into five chapters. The review of graphene and graphene-related materials including experimental and theoretical work is presented in Chapter 2. Chapter 3 covers the theoretical background of density functional theory and its implementations. In Chapter 4, we present and discuss our results. Chapter 5 contains our concluding remarks.

2

Literature review

2.1 Background of carbon material

Carbon was discovered by early human beings as charcoal and was named by A.L. Lavoisier in 1789 [2]. It is widely distributed in nature. Carbon is found in planatery bodies such as stars, the sun etc. It exists in several allotropes such as diamond, graphite, carbonnanotubes and more lately graphene. All allotropes of carbon are thermodynamically stable and require a high temperature before they can react[2]. Carbon exhibits a variety of interesting structural and electronic properties because of its propensity to form both sp^2 and sp^3 bonds[29]. This gives rise to a range of interesting magnetic, transport and physical properties exhibited by carbon and carbon-based materials - especially nanoscaled materials.

Diamond is a hard form of carbon found in the Kimberlite of ancient volcanic erosion around the world. The carbon atoms are tetrahedrally bonded to each other in the diamond. This makes the structure three dimensional and cubic. The bonding hybridization that occurs in diamond structure is sp^3. The electronic properties reveal that diamond is an insulating material with a wide band gap between the valence and

conduction bands.

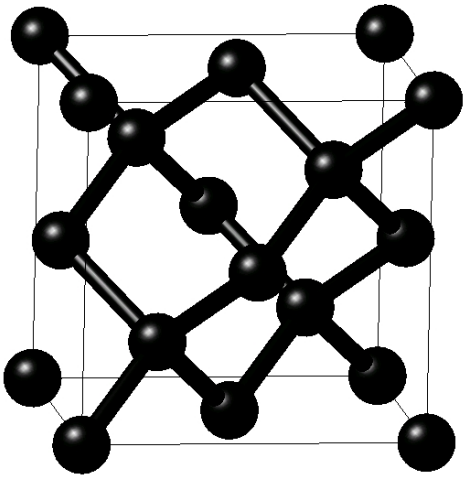

Figure 2.1: The conventional unit cell of carbon in the diamond structure

Diamond possesses strong physical properties but poor electronic ones. Diamond has a high density of 3.515 $g.cm^{-3}$ [7]. It is considered to be a hard material because of its high bulk modulus of 442 GPa and Young 's modulus of 1050 GPa [7]. Its thermal conductivity ranges from 900 to 2300$Wm^{-1}K^{-1}$ [7] which indicates poor electrical conductivity. Most applications of diamond are found to be for industrial purposes, mostly because of its hardness and low electrical conductivity. Diamond is used for grinding, drilling, polishing and cutting.

Graphite is a soft carbon material that is found in large quantities around the world. Graphite was recognised long ago by the ancient Romans and was used as a writing tool because of its black colour. In graphite, carbon atoms are bonded trigonally to three other carbon atoms in a plane. This kind of bonding makes the structure to be a two dimensional layer with sp^2 type of hybridization. These layers form graphite

when they are stacked on each other. Any two layers are loosely bonded through the weak van der Waals force and this is responsible for the softness of graphite. This force causes interactions between the covalently bonded layers. The delocalization of one of the outer electrons of each atom forms a π cloud which makes graphite an electrical conductor, but only in the plane of each covalently bonded layer. The nearest neighbour distance between carbon atoms is $1.42\mathring{A}$ and the interlayer distance is $3.34\mathring{A}$ [51] with the stacking sequence of ABAB.... The natural graphite has been determined experimentally to have an interplanar cohesive energy of 42.6 meV [51].

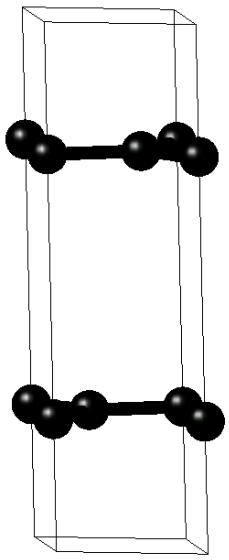

Figure 2.2: The 1x1 unit cell of graphite struture.

Unlike diamond, graphite has interesting technological applications due to its properties. Graphite possesses a low thermal conductivity which ranges from 119 to 165 $Wm^{-1}K^{-1}$ [7] and a density of 2.267 $g.cm^{-3}$ [7]. The electronic properties reveal that graphite is a semiconducting material with a narrow band gap between the conduction and valence bands. This makes graphite a promising material for technological applications.

2.2 The graphene structure

For many years, graphene was the missing allotrope of carbon, after the discovery of graphite, diamond, carbon nanotubes and fullerenes. Graphene was discovered in the late 2004 at the centre for Mesoscopic and Nanotechnology of the University of Manchester in the United Kingdom, directed by A.K. Geim and K.S. Novoselov [84, 85]. Graphene was obtained by the cleavage of a single atomic layer from a sample of graphite using a piece of sticky tape [41]. Graphene is a one-atom thick sheet of carbon atoms, arranged in a honeycomb (hexagonal) lattice and is two dimensional [8]. Graphene as one allotrope of carbon is black in colour and is a very soft material compared to hard diamond. The softness of graphene is due to the fact that it has out of plane vibrational modes (phonons) which are absent in three dimensional solids.

To date, graphene is the building block of all other modern allotropes. By rolling it in one dimension it becomes a carbon nanotube while by stacking in three dimensions, it becomes graphite and it can be wrapped to form a zero dimensional fullerene [29]. Most theoreticians doubted the existence of graphene thinking that it might be highly thermodynamical unstable until it was found that its stability is similar to that of graphite. Whenever one writes with a pencil, it releases black pieces containing graphene layers.

The first graphene membrane was produced with an area of $1mm^2$ [50]. Electrons in graphene behave as 'Dirac Fermions' and mimic the dynamics of hyper-relativistic electrons [42]. The Dirac Fermions move at a speed of $10^6 m/s$ which is 300 times less than the speed of light. They behave differently to ordinary electrons especially when exposed to a magnetic field [52]. It was observed that graphene exhibits high carrier mobilities of electrons which display unusual dependence on the concentration of impurities [42].

2.2.1 Structural properties of graphene

Graphene has a two dimensional hexagonal structure with a space group of $P6/mmm$ with the lattice vectors expressed as follows,

$$\mathbf{a_1} = \frac{a}{2}(3, \sqrt{3}), \quad \mathbf{a_2} = \frac{a}{2}(3, -\sqrt{3}). \tag{2.1}$$

The nearest neighbour distance (carbon-carbon distance) is represented by the letter a in equation (2.1) and is approximately $1.42\mathring{A}$ ($a \approx 1.42\mathring{A}$). Graphene has lattice constants of $\mathbf{a_1} = \mathbf{a_2} = 2.46\mathring{A}$ [50] and is a triangular lattice with a basis of two atoms per unit cell. When extending the graphene layer, we consider the other three next nearest neighbour vectors given by,

$$\boldsymbol{\sigma}_1 = \frac{a}{2}(1, \sqrt{3}), \quad \boldsymbol{\sigma}_2 = \frac{a}{2}(1, -\sqrt{3}), \quad \boldsymbol{\sigma}_3 = -a(1, 0). \tag{2.2}$$

There are two types of graphene structure, namely the zigzag and armchair type. These structures differ according to their orientations and the directions of the edges. By looking at figure (2.3) and considering the edge along the y axis, we see an armchair structure. Using the edge along the x-axis, we see the zigzag structure.

Bonding of graphene

Graphene, just like graphite, consists of the sp^2 hybridization of one s orbital and two p orbitals. This sp^2 makes the structure trigonal planar which causes a sigma (σ) bond between the two carbon atoms. The distance between carbon atoms in the graphene structure is $1.42\mathring{A}$[50] which is shorter than that in cubic diamond. The σ bonds occur in all allotropes of carbon and are responsible for the robustness of the lattice structure.

Graphene also contains π bond formed by the covalent bonding between two carbon

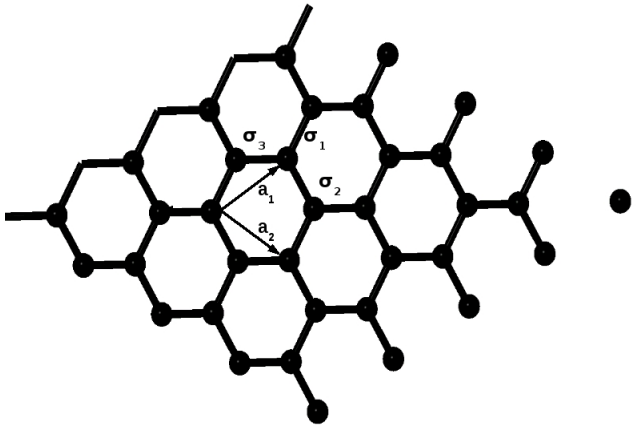

Figure 2.3: The lattice structure of graphene, made out of two interpenetrating triangular lattices (a1 and a2 are the lattice unit vectors and σ_1, σ_2 and σ_3 are the nearest neighbour vectors)

atoms and occurs in the p orbital states. This π bond is responsible for the band structure of graphene being semimetallic with the unusual linear dispersion of the Dirac Fermions [42]. The π bond shows that the graphene layer has clouds of electrons above and below which is responsible for its semimetallic nature.

2.2.2 The electronic properties of graphene

The electronic properties of a material enable us to classify materials as metals, semimetals or insulators. This classification is derived from the densities of states and band structures of the material.

2.2.2.1 The electronic band structure of graphene

Electrons in graphene have the unique property of posessing extraordinary mobility v_f which plays a vital role in the applications of graphene. The electronic structure of graphene was found to have the form of the relativistic Dirac equation which is

massless. The Brillouin zone of graphene consists of two momentum positions (Dirac points) at the corners of the zone labelled as $\mathbf{K}$ and $\mathbf{K}'$ respectively. We define their positions as follows,

$$\mathbf{K} = (\frac{2\pi}{3a}, \quad \frac{2\pi}{3\sqrt{3}a}), \quad \mathbf{K}' = (\frac{2\pi}{3a}, -\frac{2\pi}{3\sqrt{3}a}). \tag{2.3}$$

These Dirac points are presented on figure (2.4), where the gamma (Γ) point is found at the centre of the Brillouin zone and is non degenerate.

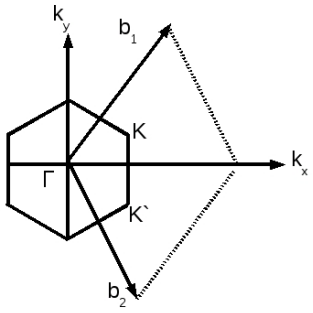

Figure 2.4: The Brillouin zone of the graphene structure.

The band structure of graphene was first studied by Wallace et al. in 1947 using the tight binding method [112]. This was done in order to research the low energy properties of graphite considering the outer layer [112]. The tight binding method is based on the Hamiltonian of the graphene being written as,

$$H = -t \sum_{n,\sigma_i} a_n^\dagger b_{n+\sigma_i} + a_n b_{n+\sigma_i}^\dagger. \tag{2.4}$$

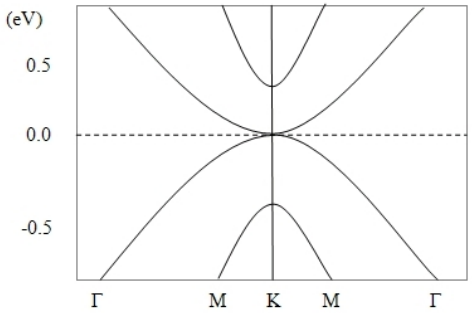

Figure 2.5: The band structure of the graphene structure.

Where t is the hopping parameter, a_n and $b_{n+\sigma_i}$ are the annihilation operators and $a^\dagger$ and $b^\dagger$ are the creation operators corresponding to sublattices of graphene. After diagonalizing the Hamiltonian equation, the operators are solved as follows:

$$a_n = \frac{1}{N}\sum_k e^{ika}a(k), \qquad b_{n+\sigma_i} = \frac{1}{N}\sum_K e^{ik(a+\sigma_i)}b(k) \tag{2.5}$$

where N is the number of primitive unit cells. Substituting the annihilation operators into (2.4) and applying the summations, we obtain the wavefunctions of graphene as follows:

$$\psi(k) = -te^{ik_x a/\sqrt{3}}[1 + 2e^{-i\frac{k_x a\sqrt{3}}{2}}cos(\frac{k_y a}{2})]. \tag{2.6}$$

Theoretically, the energy bands are derived by the eigenvalues

$$\varepsilon(K) = \pm|\psi(k)|. \tag{2.7}$$

The equation (2.8) is responsible for the theoretical calculations of the band structure of graphene materials.

$$\varepsilon(K) = \pm t\sqrt{1 + 4cos^2(\frac{k_y a}{2}) + 4cos(\frac{k_y a}{2})cos(\frac{\sqrt{3}k_x a}{2})}. \tag{2.8}$$

Figure (2.5) shows the tight binding calculated band structure for graphene from equation (2.8). We observe that the band dispersion is conical at the Dirac points, unlike that in some crystal materials which have a parabolic dispersion. The dashed line, which is called the Fermi level, lies exactly at the intersection points. This phenomenon reveals to us that graphene material is a gapless semiconductor.

2.2.2.2 The electronic density of states of graphene

Figure (2.6) depicts the theoretical DOS of graphene showing semimetallic behaviour. This DOS of graphene is completely different to that of diamond which has a wide band gap. Figure (2.6) shows that the density of states for graphene has a zero band gap between the valence and conduction band.

The density of states (DOS) is derived from (2.9) and its expression is written as follows:

$$\rho(E) = \frac{4}{\pi^2}\frac{|E|}{t^2}\frac{1}{\sqrt{Z_0}}g(\frac{\pi}{2}, \sqrt{\frac{Z_1}{Z_0}}). \tag{2.9}$$

The function g denotes the elliptic integral while Z_0 and Z_1 are the phases of the graphene. The equation(2.9) is approximated by equation (2.10) near the Dirac point.

$$E_{\pm}(q) \approx \pm v_f|q| + 0[(\frac{q}{K})^2] \tag{2.10}$$

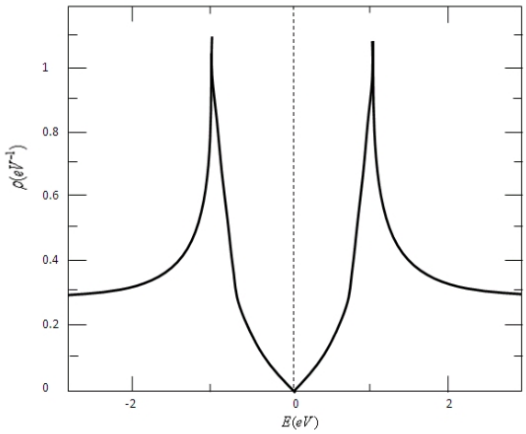

Figure 2.6: The density of states of the graphene structure.

The function q is the momentum obtained relative to the Dirac points. This approximation reduces the DOS of graphene to

$$\rho(E) = \frac{2A_c}{\pi}\frac{|E|}{v_f^2} \tag{2.11}$$

per unit cell.

2.2.3 Physical properties and possible applications of graphene

Since the discovery of graphene, several experiments have been done revealing remarkable properties. These properties indicate that graphene is versatile and scalable in a variety of applications.

Graphene was reported to have a high Young's modulus of $1.100GPa$ [102] and a fracture strength of $125GPa$ [36]. It possesses a thermal conductivity of $5000Wm^{-1}K^{-1}$ [13]. The thermal conductivity depends on the lateral dimensions of the graphene flakes. The surface area, which was measured by Stoller et al., was found to be $2.630m^2g^{-1}$ [106]. The above properties were measured at room temperature ($300K$) and are suitable for graphene to be used in nanotechnology applications. Graphene can be used as a gas sensor due to the fact that it possesses unique electron properties, which are easily affected by gas molecules touching the graphene surfaces.

Graphene can also be used as a support membrane for transmission electronic microscopy. This is due to the fact that the fracture strength and the Young's modulus of graphene make it very strong with bonds that are not easily broken. Graphene can also be used to hold micro and macroscopic objects (nanoparticles, DNA) to make them visible through an electron microscope. In addition, graphene is made out of carbon atoms only which will be simple to differentiate from other material during observation.

Graphene is useful in transistor production because it is a thin material. This makes controlling the conduction easier when applying an electric field to the material. The speed V_f of the electrons in the graphene enables the transistor to run at high frequencies. This offers the possibility of fabricating a graphene based integrated circuit (IC). Graphene is also not easily reactive with acids and alkalines and is a possible candidate for inert coatings to protect objects such as metals from these reagents.

2.3 Review of experimental work on graphene

In this section we review the experimental preparation of graphene and its properties. When doing so we discover that the key instruments employed to study graphene layers

are the scanning tunnelling microscope (STM) and Raman spectrometer.

2.3.1 Preparation of graphene

Currently graphene has been prepared using three different techniques i.e, micromechanical cleavage of graphite [84], the epitaxial growth on SiC substrates [16] and Hummers method[61]. The micromechanical cleavage of graphite is used to obtain high quality graphene but is restricted to small sample dimensions and low visibility. The epitaxial growth on SiC substrates can produce a large amount of graphene in a small period of time but the quality still needs to be improved.

Our focus is on the Hummers method [61], which requires the sample to be transferred to an insulating substrate in order to make useful devices. This method involves pre-exfoliation of graphite by microwave heating. The heating expands the graphite into a thinner layered structure. This approach produces a high amount of large single layer graphite up to $0.002m^2$ in size in a smaller period of time. The small amount of expandable graphite is sealed in a glass vial and purified with a high quantity of nitrogen for 2 hours [45]. The glass vial is then placed in a microwave oven and heated for less than two seconds [73]. The pieces of graphite are carefully checked to ensure that all of them have fully expanded. Those which did not expand are isolated. Five grams of $K_2S_2O_8$ and P_2O_2 are dissolved in 30 ml of concentrated sulphuric acid at a temperature of about 90°C. The expanded graphite is added to this solution and stirred at a temperature of 80°C for 4 hours.

The mixture is then added to de-ionized water and filtered through a 0.2 micron Nylon Millipore filter. The filtrated mixture is washed with water until the pH level is neutral. The light and soft graphite oxide is dried in air at 60°C for 3 hours and then mixed with 100ml of concentrated sulphuric acid. This mixture is placed in ice

cubes. After a while, $60g$ of $KMnO_4$ is added slowly to the solution until it dissolves completely. The solution is placed in a microwave at the temperature of 35°C for 2 hours and added to 1000 ml of de-ionized water, then stirred for two hours.

Hydrogen peroxide H_2O_2 is added gently to the solution and the solution is left for 24 hours at ambient temperature. The solution is then separated leaving the sediments at the bottom of the container. The remaining solution is then centrifugated and washed with 10% HCl solution three times and washed again ten times with deionized water. After washing, the remaining product is the graphene oxide which is a very viscous and brownish transparent solution. The corrosive ions are removed by dialysing against deionized water, applying a tubing process with a 12,000MW cutoff. In order to obtain pure graphene, 10mL of 98% hydrazine solution is added into 10mL of graphene Oxide product. The solution is then placed at a temperature of 50°C for 12hours. The graphene flakes are then obtained through filtration and washed with deionized water.

2.3.2 Scanning tunnelling microscope (STM) and scanning tunnelling spectroscopy (STS)

The scanning tunnelling microscope was invented by Russell Young [118] in 1965 and was further developed in 1981 by Gerd Binning and Henrich Rohrer [17] in Zurich. In 1977 they were awarded the Nobel Prize in Physics. The STM is regarded as a powerful tool for obtaining images of surfaces at the atomic scale. The STM senses the corrugations in the electron density of the surface that indicate the location of atoms. It operates when the surface is $0.1nm$ lateral and $0.01nm$ in depth [9]. The STS is also known as a counter of electrons, and is the method employed on STM to observe the local density of states and the surface of the materials [86]. This method observes the changes in the current topograph with a tip-sample bias and measures the tunnelling conductance dI/dV.

2.3.3 Application of STM and STS to graphene layer

In this section we review the STM and STS applied to graphene layers to analyze the band gap. We reviewed in detail the two types of graphene used (i.e pristine and rotated graphene where STM and STS were successfully applied).
Stolyarova et al. [43] used the STM to examine the single layer graphene crystal under high ultravacuum conditions. Their analysis reveals that graphene sample is highly conductive, since the tunnelling of electrons occurs between the STM tip and the graphene layer. In other words the graphene layer consists of a cloud of electrons which indicates the conductivity of the material. This concept was first revealed by Elias et al. [38]. When measurements were conducted, the sample potential bias was set at $1V$ and the tunnelling current was chosen to be $1nA$. The voltage must be high in order to avoid the structure becoming unstable. Their STS images clearly show the hexagonally symmetric honeycomb structure without any defects present. Stolyarova et al. [43] concluded that the whole layer consists of atoms contributing equally to the tunnelling images.

Vital et al. [110] used the STS at low temperature to investigate the local electronic structure of mono-layer graphene. They made use of a rotated layer with a periodicity of $(6\sqrt{3}X6\sqrt{3})R30^{\circ}$ in the interface structure. The STS image observed by Vital et al. exhibits two peaks at energies close to the Dirac point which indicates that the π bands are separated by an energy gap. They discovered that the Dirac point, as determined by the median of two π bands, is shifted with respect to the Fermi level by about -460 MV. Their STM measurement reveals that the peak positions vary in energy according to the periodicity of the interface structure and that the gap size was found to be 220 mV. The STM image for structural characterisation reveals some defects on the structure which is contrary to the observation of stable graphene by Stolyarova et al.

2.3.4 Raman microscope and spectroscopy

The Raman effect was observed by Sir C.V. Raman in 1928 in India [49]. Two years later he was awarded the Nobel Prize in Physics [49]. Raman Spectroscopy is the method used to investigate how systems vibrate and rotate [4]. It depends on the inelastic scattering (sometimes called the Raman scattering) of mono-chromatic light. This mono-chromatic light is generated by a laser in the ultraviolet range. Its purpose is to interact with phonons in the material. In solid state, Raman spectroscopy is also used to orientate samples and characterize materials. Raman spectra can be obtained from both molecular samples and some metals [64].

2.3.5 Raman spectroscopy applied to graphene

It was found that in most investigations, Raman spectroscopy produces both qualitative and quantitative results [3]. It has been applied to graphene single layers, bilayers etc by different researchers. Some of their results are discussed below and were of quality to allow the layer to be investigated thoroughly.

Zhenhua et al. [82] used the Raman spectroscopy to study the following: (i) determine the number of graphene layers, (ii) determine the strong signal of graphene on a SiO_2/Si substrate in terms of peaks, (iii) investigate the effect of substrates on the physical and electronic structure of graphene and (iv) investigate epitaxial graphene on an Sic substrate. They started by applying Raman spectroscopy to compare graphene and graphite on an SiO_2 substrate. The laser power was set to be less than 0.1mW in order to avoid heating the sample. The Raman signal of graphene was found to be strong and comparable to that of graphite. The major Raman frequency of graphene and graphite was found to be $1580cm^{-1}$ for the G-band and $2670cm^{-1}$ for the 2D band. The G-band originates from in-plane vibrations of sp^2 carbon atoms and is a double degenerate phonon mode at the centre of the Brillouin zone [94].

The 2D band originates from a two phonon double resonance Raman process and is closely related to the band structure of graphene layers. The only difference observed by Zhenhua Ni et al. [82] for the Raman spectra is on the 2D band spectra: for graphene the 2D band is fitted with a sharp peak while for graphite it is fitted with two peaks. However the 2D band becomes broad when the graphene thickness starts to increase from one layer to multi layer graphene. A feature of Raman spectroscopy in determining the number of layers is that it does not depend on the substrate used.

Park et al. [87] measured the Raman spectra from single to triple layers of graphene as a function of laser excitation energy. They observed that the G-band Raman peak of $2650cm^{-1}$ intensity decreases with the increases in the number of graphene layers. Their Raman intensity calculations show that each peak position depends on its wavevector. They suggest that the G-band of two layers graphene can be described by two components and three layers graphene with five components. This phenomenon is due to the fact that the split width of the energy band near the Fermi level depends on the interlayer distance, which they fixed at 0.34 nm.

The interlayer distance decreases with the increase of the energy band [46]. Their results show that the increament from one layer to two layers decreases the G band frequency from $20cm^{-1}$ for two layers to $10cm^{-1}$ for three layers. Their conclusion was that the G band width of graphite is less than the G band width of two layers graphene and that the G peak intensity depends on the laser excitation energy which is predicted to decrease with the decrease in the electron photon matrix element.

2.4 Review of first principles work on graphene

The discovery of graphene by Novoselov et al. [84] in 2004 has caused much interest in these unique two dimensional systems because of the enormous potential in exploiting the electronic, magnetic and optical properties. These systems also provide theoreticians with the opportunity to explore novel methods for modelling these systems because of their ideal two dimensional nature. A great effort recently has been centred on altering the electronic structure of graphene using various dopants to generate the band gap. Hydrogen is the most frequently used choice of dopant in modelling as was evident in experiments.

Leenaerts et al. used the ABINIT software [44] employing GGA for the exchange correlation potential [91]. The pseudopotential used was the Troullier-Martins type [108]. Leenaerts et al. [75] investigated the adsorption of two different molecules on a graphene namely ammonia (NH_3) and nitrogen dioxide (NO_2). For the adsorption of NH_3, they looked at its two different orientations on the graphene surfaces. In the first orientation, all hydrogen atoms are pointing up away from the surface while in the second all hydrogen atoms are pointing downwards to the surfaces. Their observations were that there was a small charge transfer of $0.03e$ from the ammonia to the graphene layer in the upwards orientation whereas in the case of the downwards orientation, the charge transferred was found to be zero.

Leenaerts et al. [75] explained this phenomenon in terms of highest occupied (HOMO) and lowest occupied (LUMO) molecular orbitals of NH_3. In the upwards orientation of NH_3 the HOMO and LUMO of the molecule are close to the Dirac point which causes charge transfer through hybridization with graphene orbitals. In the case of the downward orientation, both HOMO and LUMO of the NH_3 are able to interact with

graphene which leads to competing charge transfers to and away from the graphene layer, leaving an absence of net charge transfer. They concluded that the upwards orientation is favoured, energetically speaking. They compared the amount of charge transferred for an upward orientation with the value obtained for a carbon nanotube (CNT) of $0.04e$ investigated by Bradley et al. [21] and their value was less.

For the adsorption of the NO_2 molecule, Leenaerts et al. [75] examined different orientations: N-O pointing upwards followed by N-O pointing downwards. In all orientations, they obtained values of charge transfer higher than the value of ammonia on graphene. They observed that in all orientations charge transfers occur. Their highest observed value was found to be around $0.102e$ less than the experimental value of $1e$ obtained by Schedin et al [99]. All calculations were performed on a 4x4 graphene supercell with a distance of $16\mathring{A}$ between adjacent layers. Leenaerts et al. decided to perform the same type of calculation, varying the size of the supercell to check the size effects on the charge densities. They observed an increase in charge transfer with an increase of the supercell sizes. Their conclusion was that the charge transfer may be very large, depending strongly on the size of the supercell used.

Denis et al [34] investigated the adsorption of hydrogen on perfect graphene and stone whale defect graphene (one carbon being rotated upto 90°) using the Siesta code [105]. They employed supercells sizes of 4x4 and 5x5 having 32 and 50 atoms respectively. They optimized the unit cell along the **a** and **b** directions while the **c** parameter was set to $30\mathring{A}$ to prevent interaction between adjacent sheets. Their structural properties reveal a depucking height of $0.49\mathring{A}$ more than the one obtained by Casolo et al. [25] by only $0.01\mathring{A}$ and the distance between carbon and hydrogen was found to be $1.138\mathring{A}$. The hydrogen carbon distance for perfect graphene was found to be larger than that for stone whales graphene sheet, which is $1.127\mathring{A}$. The binding energy of perfect

graphene was found to be less compared to the one for stone whales graphene. They concluded that the stone whales defect is highly reactive with hydrogen and which was also confirmed by Meyer et al [80].

Denis et al. [34] plotted the electronic density of states which indicated that for both pristine graphene and stone whales graphene there exists a zero band gap. In the case of adsorption of hydrogen on both layers modification was observed: in the case of pristine graphene the band gap was opened even though the peak was observed at the centre of the gap, revealing that the structure was not fully saturated. A different observation occurs in the stone whales graphene where the electronic structure reveals metallic properties. Their conclusion was that in both sheets, higher hydrogenation is needed to induce a band gap.

Roman et al. [96] employed the Dacapo software [54] to investigate the pairing of hydrogen adatoms on graphene. Dacapo implements a supercell approach to density functional theory using ultrasoft pseudopotential for the frozen core atoms. A pair of hydrogen adatoms was adsorbed on a 4x4 graphene supercell and a geometry optimisation option calculation was employed to give the hydrogen adatom complete degree of freedom. Their binding energy calculations reveal that the graphene contains two different sublattices. The first sublattice is stable but the other is not. This was found to be in agreement with the work done by Hornekaer et al. [60] and Andree et al. [12] for the adsorption of deuterium.

Chan et al. studied the equilibrium properties of a single isolated Li adatom on graphene [27]. They considered a (4x4) conventional cell, which they argued was sufficiently large to minimize adatom-adatom interactions. They found that the hollow site, with a binding energy of $1.096eV$, was energetically most favourable, followed by the bridge site, with a binding energy $0.773eV$, itself followed by the ontop site with a

binding energy of $0.754eV$. Furthermore, Chan et al. concluded that the binding was ionic in nature with charge being transferred from the Li to the graphene substrate with no significant change to the occupied graphene bands.

Chih-Kai Yang [30] calculated the binding energies of Li adatoms adsorbed on the graphene employing (1x1) and 2x2 cells. He considered Li adatoms alternating above and below the graphene layer [30]. After a careful analysis, Yang concluded that the (1x1) cell was adequate to describe this system. Yang found the counter-intuitive structure, where the C atoms are pushed into the plane, a direct reversal of the situation in graphane where the H adatoms are responsible for pulling the C atoms out of the plane. Yang found strong metallic behaviour in this case, involving Li on graphene with a peak in the electronic density of states at the Fermi level.

3

Theoretical background

3.1 Electronic structure calculations

In order to describe the properties of crystals from first principle methods, we need to know the Hamiltonian of the system consisting of the number of electrons and nuclei:

$$H = -\hbar^2 \sum_i \frac{\nabla_i^2}{2m} - \hbar^2 \sum_I \frac{\nabla_I^2}{2M_I} + \frac{1}{2} \sum_{i \neq j} \frac{e^2}{|r_i - r_j|} - \sum_{i,j} \frac{Z_i e^2}{|r_i - R_I|} + \frac{1}{2} \sum_{I \neq J} \frac{Z_I Z_J e^2}{|R_I - R_J|} \ . \tag{3.1}$$

Where r_i denotes the position of the ith electron, R_I is the position of the Ith nucleus, Z_I is the atomic number of the nucleus. m is the mass of the ith electron and M_I is the mass of the Ith nucleus respectively. In order to accurately describe the influence of all interactions in the system, all terms are considered including the complicated electron-electron and nucleus-nucleus interaction terms. Since most systems consist of a large number of atoms, it is impossible to solve the stationary Schrodinger equation for the above Hamiltonian (3.1) directly even when using the largest and fastest computers. This requires simplifications to the Hamiltonian which involves several approximations. The simplification of the Schrodinger equation is core to electronic structure theory.

The Schrodinger equation may be simplified by the development of approximations to the electronic correlations with sufficient accuracy to enable the prediction of various properties of matter. The first approximation involves the separation of electrons into valence and core electrons. The core electrons are those found in the fully occupied orbitals: e.g in the case of the carbon atom,the orbitals are as follows: $1s^2$. Such electrons occur around the nuclei and group together with the nuclei to form an ion core. In the Schrodinger equation, I and J denote the core ions and i signifies the valence electrons which occur in the incomplete orbital i.e $2s^2$,$2p^2$ in the case of carbon.

The second approximation is the Born-Oppenheimer or adiabatic approximation [20] which involves the separation of the degrees of freedom connected with the motion of nuclei from those of the electrons. The ions are much heavier than the electrons which results in the ions moving much slower compared to the latter. This makes the nuclei kinetic energy term negligible in the Schrodinger equation. This approximation reduces the many-body problem to the dynamics of the electrons with some frozen-ion configuration of the nuclei. The ion-ion interaction term is not ignored because their position can be varied in order to determine the minimum energy of the system (ground state). In this approximation the nuclei are treated classically. Their ground state is obtained as the minimum of their potential energy ignoring quantum spins. The electron kinetic energy term is

$$T_{elec} = -\frac{1}{2}\sum_i \nabla_i^2 \tag{3.2}$$

applying the Hartree atomic units where $\hbar = m_e = e = 4\pi\epsilon = 1$. The electron-ion potential is written as follows,

$$V_{ion-elec} = -\sum_{i,I} \frac{Z_I}{|r_i - R_I|}. \tag{3.3}$$

The potential energy due to electron-electron interaction is

$$V_{elec-elec} = \frac{1}{2}\sum_{i \neq I} \frac{Z_I}{|r_i - r_j|} \tag{3.4}$$

and the potential energy due to ion-ion interaction is

$$V_{ion-ion} = \frac{1}{2}\sum_{I \neq J} \frac{Z_I Z_J}{|R_I - R_J|}. \tag{3.5}$$

The Hamiltonian of the system is now reduced to

$$H = T_{elec} + V_{ion-elec} + V_{elec-elec} + V_{ion-ion}. \tag{3.6}$$

The Hamiltonian can be further modified by employing pseudopotentials that replace the ion-ion interaction potential of the core electrons.

3.1.1 Independent-electron approximation

The most important task is to solve the Schrodinger equation of a system having more than one electron even if the principles behind the calculations are well understood. There are many effects occurring in the system, i.e. electron-electron, ion-ion interactions which create many forces that causes the solution to be highly complex. Several approaches have been developed to deal with such kinds of problems, with and without success. One approach is the independent-electron approach. It assumes the electron-electron contributions can be dealt with by a clever choice of periodic potential $V(r)$ in the one-electron Schrodinger equation below,

$$[T_{elec} + V(r)]\psi_k(r) = \varepsilon(k)\psi_k(r) \tag{3.7}$$

The subscript k is a wave vector and r denotes the position of the electron. However a problem arises in describing a system of more than one electron. The potential $V(r)$ must be chosen to describe the interaction of periodic ions and the interactions of other electrons, but in order to establish this the (3.7) is needed to be solved for all other electrons first. Which means that in order to know the potential one need to know the solution, but to discover the solution one needs to know the potential: this require some methematical efforts. This leads to the failure of independent electron approximations. In 1920, Douglas Hartree [56] developed an approach named after himself called the Hartree approximation.

The Hartree approximation is capable of solving the multi-electron Schrodinger equation of the wave function of the form $\psi(r_1 s_1, r_2 s_2, ---, r_n s_n)$. This approximation defines the potential by separating it into an electron potential (V_{elec}) and an ion potential V_{ion}. During the interaction, one electron feels the electric field of other electrons. This leads to the remaining electrons being treated as a smooth distribution of negative charge with their charge density defined as follows,

$$\rho_i(r) = -e \sum_i \mid \psi_i(r) \mid^2 \tag{3.8}$$

The subscript i assumes that electrons are uncorrelated and obey the Pauli exclusion principle. The electron potential can be modified by substituting the charge density (3.8) as follows,

$$V_{elec} = e^2 \sum_i \int dr' |\psi_i(r\prime)|^2 \frac{1}{|r - r'|}. \tag{3.9}$$

Then, substituting the above equation and the ordinary ion-ion interaction potential (V_{ion}) in the equation (3.7) we obtain the Hartree equation

$$\epsilon_i \psi_i(r) = [T_{elec} + V_{ion}(r) + V_{elec}(r)]\psi_i(r). \tag{3.10}$$

The Hartree approximation fails to work when the electron is removed from the averaged N electrons, and it is only capable of describing the field experienced by the electron from the other remaining electrons but it provides good results. Improving the Hartree approximation is a difficult task. In the next section we focus on the Hartree-Fock approximation which is just the inclusion of another term called the exchange term in the Hartree equation.

3.1.2 Hartree-Fock approximation

The main purpose of the Hartree-Fock [47] approximation is to correct the failure of the Hartree approximation. This approach is also based on the independent electron approximation. The independent electron approximation is given by the sum of a single one-electron Hamiltonian as follows:

$$H_{app} = \sum_{i=1}^{N} [T_{elec} + V(r_i)]. \tag{3.11}$$

$V(r_i)$ is the one electron potential energy in the field of all the nuclei and N is the number of electrons in the system. The solution of the Schrodinger equation is a product of one-electron states and is expressed as follows:

$$\psi(x_1, ..., x_n) = \psi_1(x_1)...\psi_N(x_N). \tag{3.12}$$

Where ψ_1,ψ_2.....ψ_N are eigenstates of the one-electron Schrodinger equation. These eigenstates are orthogonal and uncorrelated due to the fact that each particle is independent of the other. The terms x_i are the combination of spin s_i and orbital co-ordinate position r_i and are written as follows:

$$x_i = (r_i, s_i). \tag{3.13}$$

The probability density of finding the electrons in the orbital co-ordinates is given by

$$\rho(x_i, x_2....x_N) = |\psi_1(x_1)|^2|\psi(x_2)|^2.....\psi|(x_N)|^2. \tag{3.14}$$

This equation is the product of one electron probability densities and is uncorrelated. A state $\psi(x_i)$ with the permutation of x_i is also a solution of the Schrodinger equation, but we require the state to be antisymmetric with the interchange of any two electrons in order to satisfy the Pauli's exclusion principle. The solution of the Schrodinger equation can be determined by replacing the trivial wave function $\psi(r)$ by a Slater determinant [103] of one-electron wave functions.

$$\psi(x_1, x_2, ..., x_N) = \frac{1}{\sqrt{N!}} Det[\psi(x_1), \psi(x_2), ..., \psi(x_N)] \tag{3.15}$$

The Slater determinant above is helpful in obtaining the exchange term $-\frac{1}{2}\sum_j \int d^3r' \psi_j^*(r')\psi_i(r')\frac{1}{|r-r'|}\psi_j(r)$ that acts between electrons of the same spin. Applying this third term to the Hartree equation leads to the Hartree-Fock equation. The latter equation is written as follows:

$$\epsilon_i\psi(r) = [T_{elec} + V_{ion}(r) + V_{elec}]\psi_i(r) - \frac{1}{2}\sum_j \int d^3r' \psi_j^*(r')\psi_i(r')\frac{1}{|r-r'|}\psi_j(r) \tag{3.16}$$

The exchange term introduces some complications to the Hartree equation and causes the Hartree-Fock equation to be difficult to solve because of its non-local nature. This results in the Hartree-Fock approximation not being an improvement as such. In some calculations it gives less satisfactory results than the Hartree approximations. This approximation fails due to the ignored Coulomb repulsion of the electrons in the approximation referred to as the correlation of the electrons. But it yields some better results for molecules and is employed in chemistry calculations for this reasons. This approximation fails to completely describe the properties of metals especially their den-

sity of states. The electrons that contribute most to metallic properties are those close to the Fermi energy, these electrons are calculated to have infinite velocities within the Hartree Fock theory. The DOS function which should closely resemble that of a free electron gas instead approaches zero at the Fermi energy.

It is therefore important to closely examine and understand density functional theory method that operates differently from the Hartree-Fock method. It is in principle an exact theory, but in practice useful approximations are derived for the exchange-correlation potential.

3.1.3 Density functional theory

Introduction

Density functional theory (DFT) is today one of the most important tools for predicting the ground-state properties of electronic systems (metals, semiconductors and insulators). The reason for the widespread use of this tool is its accuracy and high computational efficiency. The DFT started to be popular in the 1970's and in 1998, one of its creators, Walter Kohn [10], was honoured by receiving the Nobel Prize in Chemistry. To date it is still one of the leading tools for calculation of electronic structure in solid state physics and chemistry. The DFT yields results regarding electronic structure which are quite comparable to experimental results. The DFT is a different approach to the Hartree Fock method [47]. The Hartree Fock method focuses on the many body wavefunctions as the fundamental variable of the system while DFT describes the entire number of interacting electrons through their density. The Hartree Fock approximation is computationally very costly and fails particularly for metals.

DFT separates the total energy into three terms, starting with the kinetic energy term, the (coulomb energy term which includes the classical electrostatic interactions between the electrons and nuclei in the system) and the exchange-correlation term

that includes the many body interactions. Although DFT is significant, it fails to properly describe the van der Waals forces in sparse materials [1]. The DFT also underestimates the band gaps of semiconductors and some other electronic properties of highly correlated systems. It is still a current focus of improvement in research.

3.1.3.1 Basics of density functional theory

Density functional theory is based on the statement of Hohenberg and Kohn [59] in 1964 that the total energy of an electron gas enclosed in a large box is a unique functional of electron density $\rho(r)$ and that the ground state energy expectation value depends uniquely on the ground state density of the electrons. To prove the Hohenberg and Kohn statement, we need to consider the following *Theorem*: If two densities $\rho(r)$ and $\rho'(r)$ based on the two ground states of different potentials $V(r)$ and $V'(r)$ are equal i.e $\rho(r,V) = \rho'(r,V')$ then the potentials $V(r)$ and $V'(r)$ differ by a constant. Proof: Considering the above mentioned theorem, several assumptions are made. The potentials $V(r)$ and $V'(r)$ produce Hamiltonians as follows: $H = T + U + V$ and $H = T + U + V'$ respectively with their two different wavefunctions ($\psi(r)$ and $\psi'(r)$) in a ground state.

1. The ground state is non degenerate and $V(r) - V'(r) \neq constant$, with the ground state wavefunctions not identical ($\psi(r) \neq \psi'(r)$)

2. The ground state wavefunctions must be normalized $\langle\psi(r), \psi(r)\rangle = 1$ and $\langle\psi'(r), \psi'(r)\rangle = 1$. Their coresponding ground state energies are given by $E = \langle\psi(r)|H|\psi(r)\rangle$ and $E' = \langle\psi'(r)|H'|\psi'(r)\rangle$

3. The ground state density $\rho(r)$ is exact. If the wavefunction $\psi'(r)$ is not a ground state eigenstate of Hamiltonian (H) compared to the ground state $\psi(r)$ it is always

large. The ground state energy corresponding to the potential $V(r)$ is

$$E = \langle\psi(r)|H|\psi(r)\rangle < \langle\psi'(r)|H|\psi'(r)\rangle. \tag{3.17}$$

The last term can be extended by assuming the identity of the two densities :

$$\langle\psi'(r)|H|\psi'(r)\rangle = \langle\psi'(r)|H'|\psi'(r)\rangle + \int (V - V')\rho(r)d^3r. \tag{3.18}$$

We have assumed that the term $\langle\psi'(r)|H'|\psi'(r) = E'\rangle$. Then equation(3.18) is reduced to

$$\langle\psi'(r)|H|\psi'(r)\rangle = E' + \int (V(r) - V'(r))\rho(r)d^3r. \tag{3.19}$$

The strict inequality results from the variational principle whereby the wavefunction $\psi(r)$ is the ground state and is non degenerate. We now consider the same relation as above but in the case where the ground state energy is E'. The Hamiltonian operator differs only in the potentials: then the ground state energy E' is written as,

$$E' = \langle\psi'(r)|H'|\psi'(r)\rangle < \langle\psi(r)|H'|\psi(r)\rangle \tag{3.20}$$

where the first term can be expanded as follows:

$$\langle\psi(r)|H'|\psi(r)\rangle = \langle\psi(r)|H|\psi(r)\rangle + \int (V'(r) - V(r))\rho(r)d^3r \tag{3.21}$$

leading to

$$\langle\psi(r)|H|\psi(r)\rangle = E + \int (V'(r) - V(r))\rho(r)d^3r. \tag{3.22}$$

The addition of(3.19) and (3.22) yields the following inconsistent results

$$E + E' < E + E'. \tag{3.23}$$

This contradiction indicates the failure of two different potentials i.e $V'(r)$ and $V(r)$ to be produced by the same ground state density $\rho(r)$. In conclusion, since the density $\rho(r)$ determines the potential $V(r)$, it will determine the ground state energy and all other electronic properties of the material.

3.1.3.2 The Kohn-Sham equations

A year later after Hohenberg and Kohn's theorem [59], Kohn-Sham [67] continued to prove the theorem which states that the total energy of the system depends only on the electron density of the system.

$$E = E[\rho(r)] \tag{3.24}$$

Kohn-Sham [67] made their contributions in advancing the calculation of the energy of the electrons and the forces of atoms [68]. Their concern was with the difficulty of understanding the ground state kinetic energy of electrons in the system. They developed DFT in such a way that all the real electrons of a system are replaced by the effective electrons of the same mass, and charge density distribution. The DFT maps the electrons of the interacting system onto a non-interacting electronic system moving in an effective potential represented in the Kohn-Sham equations [88]. This was done in order to accurately calculate the contributions to the ground state kinetic energy of the system. The other infomation which can accurately be evaluated by this approach concerns the electronic, structural and dynamical properties of the systems. The DFT is always based on the density of an electron as a scalar function given by:

$$\rho(r) = \sum_i n_i |\psi_i(r)|^2. \tag{3.25}$$

The n_i denotes the occupation number of the eigenstate i while r is any point in real space. The electron density $\rho(r)$ can be varied by changing the wavefunction $\psi(r)$ of

the system. If the electron density $\rho(r)$ corresponds to the said wavefunction, then its total energy is the minimized energy and the whole system is in a ground state. The total energy of the system depends on the positions of the atoms and can be written as,

$$E(\rho) = T_0[\rho(r)] + V_{ext}[\rho(r)] + V_{elec-elec}[\rho(r)] + E_{xc}[\rho(r)]. \tag{3.26}$$

The ground state kinetic energy term $T_0[\rho(r)]$ is given by the sum of all contributing effective electrons in the system. All effective electrons are described by wave functions in the state i. The ground state kinetic energy term $T_0[\rho(r)]$ of all effective electrons is written as follows:

$$T_0[\rho(r)] = \sum_i n_i \int \psi_i^*(r)[\frac{-\hbar^2}{2m}\nabla^2]\psi_i(r)dr. \tag{3.27}$$

The external potential $V_{ext}[\rho(r)]$ is the electrostatic potential representing the nuclei interactions and is expressed for the entire positions of all nuclei as follows,

$$V_{ext}[\rho(r)] = \int V_{ext}(r)\rho(r)d^3r. \tag{3.28}$$

The third term is the electron-electron interactions potential,

$$V_{elec-elec} = e^2 \int\int \frac{\rho(r_1)\rho(r_2)}{|r_1 - r_2|} d^3r_1 d^3r_2, \tag{3.29}$$

which describes the repulsion between electrons in the system while e is the elementary charge of the electron. Considering the case of a non-interacting system, the total energy of the system will be given in terms of the kinetic energy $T_0[\rho(r)]$ and the external potential $V_{ext}[\rho(r)]$ ignoring the interacting terms. The ground state non interacting total energy is given by,

$$E(\rho) = T_0[\rho(r)] + V_{ext}[\rho(r)] \tag{3.30}$$

In this case the charge density $\rho(r)$ for the occupied state will be calculated self-consistency by solving the Kohn-Sham equation (3.31) below. To simplify other terms of the Kohn-Sham equation we consider the use of Hartree atomic units whereby $\hbar = m_e = e = 4\pi\epsilon_0 = 1$. The simplified Kohn-sham equation is written as follows:

$$[-\frac{\nabla^2}{2} + V_{ext}]\psi_i(r) = \epsilon_i\psi_i(r). \tag{3.31}$$

The wavefunction $\psi_i(r)$ needs to be normalized in order for the density $\rho(r)$ to satisfy the normalisation condition for the number of electrons N,

$$\int \psi_i^*(r)\psi_j(r)dr = \sigma_{ij} \tag{3.32}$$

where i and j are the eigenstates of the wavefunctions. The eigenstates are ordered according to the increase in the eigenvalues. In the case of a non-interacting system, the ground state total energy of the system is solved easily with one external potential. Then the information from the non-interacting system is applied in the situation of an interacting system. In the case of an interacting system, all the ignored terms of the total energy of non-interacting system are now fully considered and the total energy term is written as follows:

$$E(\rho) = T_0[\rho(r)] + V_{ext}[\rho(r)] + V_{elec-elec}[\rho(r)] + E_{xc}[\rho(r)]. \tag{3.33}$$

However the kinetic energy term $T_0[\rho(r)]$ is still that of the noninteracting system and the external potential $V_{ext}[\rho(r)]$ term is perturbed and generalised into effective potential V_{eff}.

$$V_{eff} = V_{ext} + V_{Hartree} + V_{xc} \tag{3.34}$$

The Hartree potential term $V_{Hartree}$ is the potential due to the interactions of electrons and is expressed as follows:

$$V_{Hartree} = e^2 \int \frac{\rho(r')}{|r - r'|} d^3r'. \tag{3.35}$$

The last term (V_{xc}) is called the exchange correlation potential which is the functional derivative of exchange-correlation energy E_{xc}: it contains all the unknown contributions and is also independent of the external potential.

$$V_{xc} = \frac{\partial E_{xc}[\rho(r)]}{\partial \rho(r)} \tag{3.36}$$

Now we can write the Schrodinger equation for one electron as follows:

$$[-\frac{\nabla^2}{2} + V_{ext} + V_{Hartree} + V_{xc}]\psi_i(r) = \epsilon_i \psi_i(r). \tag{3.37}$$

This is the set of Kohn-Sham equations for an interacting system and must again obey the condition of orthonomality. So far we have described the Kohn-Sham equation in the case of non-spin-polarized material whereby the magnetic moment of the material is zero. Now we consider spin-polarized or magnetic material. Here the Kohn-Sham equation is based on the electron density for both spins,

$$\rho(r) = \rho_\uparrow(r) + \rho_\downarrow(r) \tag{3.38}$$

and the spin density σ of the material. The spin density of the material is the inclusion of both spins, up and down. Some of the terms in the effective potential depend on the spin density, especially the exchange correlation potential V_{xc}. The spin-polarized Kohn-Sham equation of an interacting system is expressed as follows:

$$[-\frac{\nabla^2}{2} + V_{ext} + V_{Hatree} + V^\sigma_{xc}]\psi^\sigma_i(r) = \epsilon^\sigma_i \psi^\sigma_i(r). \tag{3.39}$$

The eigenstates ψ_i and the eigenvalues ϵ_i also depend on the spin density $\sigma(r)$ of the material. If both spins are equal, the spin density σ vanishes for the whole system [48], which means the spin density relies on the asymmetry of the spin occupancy.

Summary of Kohn-Sham equations

The Kohn-Sham equations are solved in a self consistent manner in order for occupied states to generate a charge density that will produce the potential used in the construction of the equations. In most cases, the solution of Kohn-Sham equations is achieved successfully, once the exchange correlation energy E_{xc} is correctly approximated. The ground state total energy of the system can be obtained by minimization of the energy functional $E[\rho(r)]$ with respect to the electron density $\rho(r)$, self consistently. This is for calculating the properties of the system (insulator, semiconductor and metals). The spin-polarized Kohn-Sham equation is better than the non-spin-polarized in calculating the structural properties. The non-spin polarized is accurate in constructing the charge densities, so it is better to start with the non-magnetic calculation and followed by magnetic (spin-polarized) calculations.

3.1.4 Exchange-correlation potential

The last term of the Kohn-Sham equations (3.31) involves the exchange-correlation which includes all the remaining complicated electronic contributions. Basically we know that the electrons are indistinguishable (Fermions) which means that the wavefunctions of the many body electron system must always be antisymmetric. If they are not it means the electrons have the same spin and by the Pauli exclusion principle those electrons are avoiding each other by a certain distance which reduces the coulomb interaction. The energy gained during the reduction is called exchange energy. Considering the electrons of opposite spin, their energy difference is termed the correlation energy E_{cor}. This energy difference is caused by the small decrease in the coulomb energy

due to the small separation of the electrons of different spin caused by their charges. In terms of the explanation above, the correlation energy is always less than the exchange energy. The correlation energy helps in defining the length and the strength of interatomic bonds. In a sparse material the correlation is merely approximate since it is difficult to calculate exactly because correlation affects both kinetic and potential energy. The exchange-correlation energy is a combination of the exchange energy and correlation energy.

$$E_{xc} = E_x + E_c \tag{3.40}$$

In detailed form, the exchange corelation energy can be expresed as a function of charge density $\rho(r)$. The exchange-correlation energy has been successfully calculated by many approaches including quantum Monte Carlo methods [26], molecular dynamics methods [83] etc. Considering the situation of two electrons of opposite spin satisfying the exchange correlation principle, then the exchange correlation energy is written as follows:

$$E_{xc}[\rho(r)] = \frac{1}{2}\int\int \rho(r_1)\rho(r_2)V(r_1 - r_2)d^3r_1 d^3r_2. \tag{3.41}$$

This exchange-correlation energy $E_{xc}[\rho(r)]$ is required for evaluating the total energy $E[\rho(r)]$ of the system and is related to the exchange-correlation potential by,

$$V_{xc} = \frac{\partial E_{xc}}{\partial \rho(r)}. \tag{3.42}$$

This exchange correlation potential V_{xc} is useful in solving the density functional Kohn Sham equations.

3.1.4.1 Approximations to the exchange-correlation potential

There are several approximations to the exchange correlation, namely local density approximation(LDA), generalised gradient approximation (GGA), Meta GGA and Hybrid

functionals. In this section we focus in detail on the LDA and GGA.

Local density approximation (LDA)

In the local density approximation, the electron density $\rho(r)$ which specifies that electron density locally (over a distance comparable to the inverse Fermi wavevector k) varies smoothly. We consider the electron density $\rho(r)$ at each point r in the system and assume that: the electron at that point r experiences the same effect from the combination of the surrounding electrons as if the density of the surrounding electrons had possessed the same values throughout the entire space. We may approximate the exchange-correlation energy as the summation (integral) of the electron contribution from a volume which depends on the electron density $\rho(r)$

$$E_{xc} = \int \rho(r)\epsilon_{xc}[\rho(r)]d^3r. \tag{3.43}$$

Where ϵ_{xc} is the exchange-correlation energy per particle of a homogenous electron gas which can successfully and accurately be measured experimentally. From a theoretical point of view, ϵ_{xc} is parameterized by Hedin and Lundqvist [57]. In some of the work where LDA is applied instead of GGA, the Perdew and Zunger [89] parameterization is employed. LDA is found to be exact for transition metals due to the fact that the electron density varies smoothly. The reason that the LDA is exact is to fulfil the correct sum rule for the exchange correlation hole. The said hole is explained as electrons avoiding each other at a point r, thus obeying the Pauli exclusion principle. Their exchange-correlation energy includes the coulomb interaction of each electron

$$E_{xc}[\rho(r)] = \frac{1}{2}\int\int \rho(r)\rho_{xc}(r,r')v(r-r')d^3rd^3r'. \tag{3.44}$$

The density $\rho_{xc}(r,r')$ is regarded as the conditional density due to the fact that if the separation between these two particles approaches zero, it disappears and leaves a hole

which is called the exchange-correlation hole.

Generalized gradient approximation (GGA)

The generalized gradient approximation is another form of exchange correlation which is non local. GGA takes into account the density of the electron and its gradient at each point in the space. GGA is constructed by starting from the second order density gradient expansion for the exchange correlation hole surrounding the electron in a system by slowly varying the densities [74, 14]. It is exceptionally successful for small molecules but fails for delocalized electrons in simple metals. It takes a form which includes the gradient density

$$E_{xc} = \int \epsilon_{xc} f[\rho, \nabla\rho]\rho(r)d^3r. \tag{3.45}$$

This equation depends only on the general feature of the real space construction where f is a parametrized analytic function, and ∇ is the gradient density of the electrons. The equation above is only based on the systems of non-spin electrons. If we consider the system containing electrons with different spins, the system exhibits magnetism and is a straightforward spin polarised material. Now the equation above will take the form of spin densities,

$$E_{xc}[\rho_\uparrow, \rho_\downarrow] = \int \epsilon_{xc} f[\rho_\uparrow, \rho_\downarrow, \nabla\rho_\uparrow, \nabla\rho_\downarrow]\rho(r)d^3r. \tag{3.46}$$

GGA in most cases improves upon the LDA in the description of atoms and solids [90] and it also tends to improve the total energies and atomization energies [119, 55]. The local density approximation (LDA) underestimates the lattice constants by 1% while the GGA overestimates the lattice parameters by 1%. It also reduces the chronic overbinding of the local density approximations [66]. It tends to improve the energy band gap between valence and conduction bands in the cases of semiconductor and

insulator materials [114]. The genaralised gradient approximation is efficient in computational cost and is numerically accurate and reliable. We can conclude that GGA tends to satisfy the demands of quantum mechanics and solid state physics.

3.1.4.2 Solution of the Kohn Sham equation:the self-consistency iteration procedure

When constructing the Kohn-Sham equations of the system, firstly the wavefunctions that construct the electronic charge $\rho(r)$ must be known. These wavefunctions are the solution of the Kohn Sham equation, which means the estimated solution of the Kohn-Sham problem must be known before it can be solved. This problem can be solved iteratively by several steps.

The geometries of the system for density functional calculation are constructed using experimental bulk lattice constants, atomic positions and cell angles. Sometimes even the results from previous first principle calculations are used. The electronic density is constructed from the wavefunction and even in the case of a spin polarized wavefunction, the involvement of involving structural geometries is the fundamental requirement in defining the Kohn-Sham equation of the system completely. From the Kohn-sham equation, the Poisson 's equation is constructed and solved in order to obtain the electrostatic Coulomb potential.

Subsequently explicit form of the exchange correlation potential is used and the exchange correlation operator is constructed. Taking into consideration this variational basis set $\{\phi_j\}$, the Hamiltonian H_{ij} and overlap matrix S_{ij} elements are calculated. Subsequently the matrix $H - \epsilon S$ is diagonalized. The diagonalization equation involves

unknown coefficients as follows,

$$(H - \epsilon S)c_{ij} = 0 \tag{3.47}$$

which result in a set of one particle eigenvalues with their corresponding coefficients c_{ij} of expansion. The coefficients of expansion produce the related wavefunction as follows,

$$\psi_i(r) = \sum_j c_{ij}\phi_i(r) \tag{3.48}$$

which are then used to construct the electron density $\rho(r)$. The constructed electron density is called the output electron density. If the output electron density is not equal to the input one, it will be used as an input and the procedure explained above is repeated self-consistency until the output density is the same as the input. This is known as the self consistent field cycle (SCf). The resulting electron density is used in calculating the total energy of the system $E[\rho(r)]$ since it was proved in the previous chapter that the total energy of the system depends on the electron density of that system. The forces $F_r = \frac{\partial E}{\partial r}$ of the atom in the system can also be calculated using the output charge density.

3.1.5 The Plane wave formalism

In a solid or crystal, the wavefunctions $\psi(r)$ of the free electrons can be extended in terms of plane waves. By ignoring the potentials causes by ions, the plane waves become exact solutions of the Kohn Sham equations. An atom possessing one electron has a potential which is relatively smooth and is treated as a perturbation. Taking the example of the hydrogen atom which has potential $\frac{-1}{r}$, its wavefunction diverges at the origin and decays exponentially with increasing distance. However in systems containing more than one atom their wavefunctions in the core states are highly complicated and the potential is not smooth. Because of such complications, the plane waves

become difficult to implement due to the requirements of the plane wave components. Two types of plane waves that are used, Augmented and Orthogonalised.

The augmented plane wave is based on the solution of the Schrodinger [100] equation for the atom with a spherical region around it. This solution to the atomic problem was implemented in 1937 by Slater [103]. The augmentation solution of the augmented plane wave solution assumes the potential to be symmetric inside the spheres and zero outside. The construction of the augmented plane wave makes it identical to the original plane wave outside the sphere. The augmented plane wave solution is constructed so that its wavefunction is continuous at the radius $r = R$ whereby,

$$\phi(r) = e^{ik.r}. \tag{3.49}$$

Since the wavefunction is continuous at $r = R$, the requirements of the Schrodinger equation of the system are not clearly met and its wavefunctions do not join smoothly. The expansion of the augmented plane waves gives the correct approximation of the system 's Schrodinger equation. The wavefunction of the expanded augmented plane waves can be written in terms of the reciprocal lattice vectors G

$$\psi(r) = \sum_{G} c_G \psi_{k+G}(r). \tag{3.50}$$

This plane wave is the one which is applicable in most computational calculations nowadays and is highly accurate in terms of energy values. The second type of plane wave is the orthogonal plane wave which was introduced by Herring in 1940 [58]. This method is not accurate because it lacks the other terms but is better in approximating the bands in the materials, especially in sp-bonded metals.

3.1.6 Crystal Lattices

Crystalline solids can be described as a Bravais lattice in which small units are repeated in a periodic array. The units may be atoms, ions or molecules and the crystal may be described as primitive, Wigner-seitz, conventional unit cells etc. This crystalline solid can contain a large number of electrons (approximately 10^{23}) moving in a field produced by a similarly large number of ions. This large number of electrons is extremely difficult to use in computations. Bloch's theorem is employed to reduce this large number to as little as half the number of electrons in the unit cell of the crystal.

3.1.6.1 Bloch's theorem

The Bloch's theorem can be stated as follows: in a periodic solid, the eigenstates $\psi_i(r)$ of an electron are given in the form of plane waves times the cell-periodic $g_i(r)$,

$$\psi_i(r) = e^{ik.r} g_i(r). \tag{3.51}$$

The Bloch's theorem introduces wave vectors k which are always in the primitive cell of the reciprocal lattice and satisfy the expression $e^{ik.r} = 1$ for all lattice points. The potential $g_i(r)$ is cell periodic and can be expressed as a fourier expansion of plane waves whose wave vectors are reciprocal lattice vectors of the crystal

$$g_i(r) = \sum_q c_i, q e^{iq.r}. \tag{3.52}$$

Where q is the reciprocal lattice vectors defined by the reciprocal of lattice vector l as follows,

$$q.l = 2\pi n \tag{3.53}$$

and n is any integer. Now each electronic wavefunction can be expressed as the sum of

all plane waves,

$$\psi_i(r) = \sum_q c_{i,k+q} e^{i(k+q).r}. \tag{3.54}$$

The $c_{i,(k+q)}$ are the coefficients for the plane waves that need to be solved and depend on the kinetic energy cut-off.

3.1.7 The plane wave energy cut-off and representation of the Kohn-Sham equations in reciprocal space

In a crystal, the wavefunction at each k-point can be expanded as a plane wave basis and the convergence of kinetic energy cut-off E_{cut} can be obtained. This convergence with respect to energy is illustrated by figure (3.1)

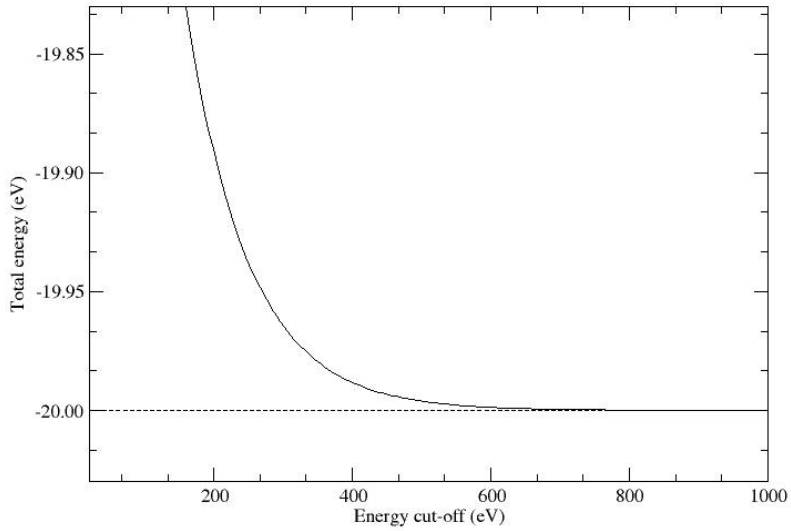

Figure 3.1: An illustration of the convergence energy with respect to energy cut-off

The Fourier coefficients $C_{i,(k+q)}$ with small kinetic energies are large and become small when the kinetic energy increases. The plane wave expansion can be truncated to

contain the plane waves that consist of the kinetic energy less than the energy cut-off.

$$\frac{\hbar^2}{2m}|k+q|^2 < E_{cut} \tag{3.55}$$

However the truncation of the plane wave expansion at a small energy cutoff will lead to an error when computing the total energies of the system. This error may decrease when the energy cut-off increases. The expansion of the electronic wavefunctions in terms of the plane waves basis set allows the Kohn-Sham equations to be represented in a reciprocal space. The electronic wavefunction expressed in terms of all plane waves equation (3.54) is substituted into the Kohn Sham equation (3.31) and, integrated over the region **r**, gives the equation

$$\sum_{q'}[\frac{\hbar^2}{2m}|k+q|^2\sigma_{qq'} + V_{ion}(q-q') + V_H(q-q') + V_{xc}(q-q')]c_{i,k+q'} = \epsilon_i c_{i,k+q'}. \tag{3.56}$$

In this equation (3.56), the kinetic energy is diagonal and the potentials are expressed in terms of their Fourier components. The Hamiltonian matrix in the square brackets of this equation (3.56) is diagonal: the size of the matrix was determined by the energy cut-off

$$E_{cut} = \frac{\hbar^2}{2m}|k+q|^2. \tag{3.57}$$

3.1.8 k-point sampling

The first Brillouin zone can be mapped out by a continuous set of k-points throughout the region of reciprocal space. These k-points represent the localies where the electronic states are found in a solid system. If there is an infinite number of electrons in a solid system there exists an infinite number of k-points in the Brillouin zone. In the calculation, the basis sets are required to represent the wavefunctions at a finite number of k-points. However the basis sets calculations are still infinite even if the energy cut-off is chosen to be very small. In the previous section, we discussed Bloch's

theorem which enables us to consider a finite number of wavefunctions in the unit cell at an infinite number of k-points within the Brillouin zone.

The electronic states calculated at a set of k-points contribute to the electronic potential of the solid system and are determined by the shape of the Brillouin zone. This is done since the electronic wavefunctions at the k-points that are close together will be identical, which causes the electronic wavefunctions to be represented over a region of reciprocal space at a single k-point. This enables us to calculate the electronic potential and the total energy of the solid system at a finite number of k-points. The error occurring during calculations can be made small by choosing a heavier set of k-points in the Brillouin zone. For example in a metallic system, dense k-points are needed since it is very difficult to define the Fermi surface with a few points. The dense k-points still make the computational time lenthly and still offer a challenge in research.

Special k-points method in the Brillouin zone

Now we consider the special k-point method of choosing the sets of points in the Brillouin zone, which makes the calculation simple and accurate. This method is based on an integrated function (3.58) averaged over a Brillouin zone.

$$F(r) = \frac{\Omega}{(2\pi)^3} \int_{BZ} f(k) d^3k \tag{3.58}$$

where $f(k)$ is the Fourier transformation of $F(r)$ and the function represent complete symmetry of the lattice. The expression Ω is the volume of the unit cell. The Fourier transform may be written in terms of $A_m(k)$ as follows:

$$f(k) = f_o + \sum_{m=1} A_m(k) \tag{3.59}$$

where $A_m(k)$ is the transformation expression defined by ,

$$A_m(k) = \sum e^{ik.r} \tag{3.60}$$

where m is any integer. The expression $A_m(k)$ is associated with any shell of the lattice vector and is a real function. This method obtains an approximate value for the integral in the equation F(r). The approximated value can be exact if the term $A_m(k)$ is zero,

$$A_m(k) = 0. \tag{3.61}$$

These sets of points are identical with the ones generated by Monkhorst and Pack [81], and this method is an unbiased one for choosing the set of k-points for sampling the Brillouin zone in fractional co-ordinates. It gives the points in a rectangular grid of points, i.e (k_x, k_y, k_z). The Monkhorst and Pack k-points are sometimes called k-meshes. When the k-meshes are large, the sampling is expected to be fine and accurate. The selection of points depends on the type of crystal. Simple cubic has k-points different to those of body centred cubic (bcc). In the face centred cube (fcc) structure, a good choice for starting points $k = (k_x, k_y, k_z)$ is to select $(\frac{1}{2}, \frac{1}{2}, 0)$ and $(\frac{1}{2}, \frac{1}{2}, \frac{1}{2})$. These chosen points can satisfy the expression $A_m(k)$ for the infinite set of nearest-neighbour shells represented by the lattice vectors.

3.1.9 Atomic pseudopotential approximations

Overview of the atomic pseudopotential

The atomic pseudopotential approximation causes the wave function to be expanded employing the basis set of plane waves. This phenomenon occurs when the strong potential of the nucleus and the effects of the tightly bonded core electrons are replaced by an effective ionic potential acting on the valence electrons. This approximation allows

the expansion of the wavefunctions to be possible using smaller plane waves, no matter how bounded the orbital is [92]. This permits the calculation to require small amount of computational time in order for convergence to be reached. The atomic wavefunctions are eigenstates of the atomic Hamiltonian, which causes the atomic wavefunctions to be orthogonal: this is illustrated in figure (3.2) where the pseudo wavefunctions oscillate

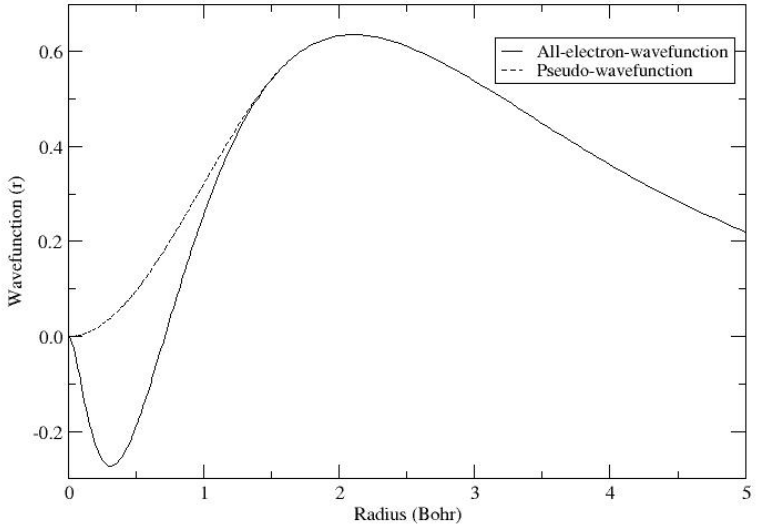

Figure 3.2: An illustration of the pseudopotential for valence wavefunction of silicon 3p electrons

less compared to the original wavefunctions. This requires a smaller number of plane waves than the original wavefunctions. The pseudo wave functions appear to be very smooth within the core region and are applicable to quite number of systems.

3.1.9.1 The projector augmented wave (PAW) pseudopotential method

The projector augmented wave method was first introduced by Blochl [19] in 1994. This method improves on the norm conserving [109] and ultrasoft pseudopotential methods [53]. The advantage of the PAW method is that it is very computationally

efficient and accurate compared to ultrasoft pps but it is complex to implement. The PAW method is based on a transformation, that maps the physically all electron (AE) valence wavefunctions onto non-interacting pseudo wave functions [78]. The transformation is designated by the character τ.

This transformation completely transforms the shape of the Schrodinger equation wavefunction into the image of Heisenberg [19]. The transformation is assumed to be unity $\tau = 1$ unless the atom is centred on the nucleus.

$$\tau = 1 + \sum \tau_o \tag{3.62}$$

The wavefunction of the system is characterized by two different features: the smooth wave function at the valence (bonding) region and the oscillating wavefunction around the nucleus. The oscillation of the wavefunction is caused by the attractive potential of the nucleus. In the PAW method, the Bra and Ket notations are used whereby the wave function $\psi_i(r)$ is denoted in terms of ket $|\psi_i(r)\rangle$ and its complex conjugate $\psi_i^*(r)$ is denoted by the Bra notation $\langle\psi_i(r)|$. The smooth wavefunctions are differentiated by tilde ($\sim$) from the all electron wavefunctions and are written as

$$|\widetilde{\psi}_i(r)\rangle = \sum_i c_i |\widetilde{\psi}_i(r)\rangle. \tag{3.63}$$

The corresponding all electron wave functions are

$$|\psi_i(r)\rangle = \sum_i c_i |\psi_i(r)\rangle. \tag{3.64}$$

The coefficients c_i are identical in both expansions and are the scalar products of the smooth wave functions

$$c_i = \langle \widetilde{P}_i | \widetilde{\psi}_i \rangle \tag{3.65}$$

for the linear transformation τ. The transformation from the smooth electron wave function to the all electron wave function is as follows,

$$|\psi_i(r)\rangle = \tau|\widetilde{\psi}_i(r)\rangle. \tag{3.66}$$

After the transformation, the full wave function in the entire space is expressed as follows,

$$|\psi(r)\rangle = |\widetilde{\psi}\rangle - \sum_i c_i[|\psi_i\rangle - |\widetilde{\psi}_i\rangle]. \tag{3.67}$$

Substituting the coefficients c_i in equation (3.67) the full wavefunctions becomes,

$$|\psi(r)\rangle = |\widetilde{\psi}\rangle - \sum_i (\langle \widetilde{P}_i|\widetilde{\psi}_i\rangle)[|\psi_i\rangle - |\widetilde{\psi}_i\rangle]. \tag{3.68}$$

The above mentioned transformation can be determined by the following: the all electron partial waves $|\psi_i(r)\rangle$ are obtained radially by integrating the Schrodinger equation of the atomic energy and the orthogonalization of the core states. The smooth partial wave function, which coincides with the coresponding all electronic partial wave function, and the projector function $|\widetilde{p}_i\rangle$ for the smooth partial wave function obeys the relation

$$\langle \widetilde{p}_i|\widetilde{\psi_j}\rangle = \sigma_{ij} \tag{3.69}$$

and is localized in the augmentation region. However in the PAW method, when varying the parameters, the smooth wave function plays a more role than the all electron function. Then the expectation value of the smooth wavefunction is needed, and is called the smooth operator and transforms the operators $(\tau, \tau^\dagger)$. The smooth operator is written as follows

$$\widetilde{A} = \tau^\dagger A\tau = A + |\sum_{i,j} |\widetilde{p}_i\rangle[\langle\psi_i|A|\psi_j\rangle - \langle\widetilde{\psi}_i|A|\widetilde{\psi_j}\rangle]\langle\widetilde{p}_i| \tag{3.70}$$

This operator is needed for evaluating the charge density and total energy of materials. The said density can be divided into smooth charge density $\widetilde{n}(r)$, which is evaluated on regular grids in Fourier or real space while the outer centre charge densities $n^1(r)$ and $\widetilde{n^1}(r)$ are evaluated on radial grids in angular momentum. The charge density at point r in real space is given by

$$n(r) = \widetilde{n}(r) + n^1(r) - \widetilde{n^1}(r). \tag{3.71}$$

The point r is the expectation value of the real space projection operator $|r\rangle, \langle r|$ while the charge density for smooth wavefunction is

$$\widetilde{n}(r) = \sum_m f_m \langle \widetilde{\psi_m}|r\rangle\langle r|\widetilde{\psi_m}\rangle| \tag{3.72}$$

whereby

$$n^1(r) = \sum_{n,(i,j)} f_m \langle \widetilde{\psi_m}|\widetilde{p_i}\rangle\langle\psi_i|r\rangle\langle r|\psi_j\rangle\langle\widetilde{p_j}|\widetilde{\psi_m}\rangle \tag{3.73}$$

and the last term is

$$\widetilde{n^1}(r) = \sum_{n,(i,j)} f_m \langle \widetilde{\psi_m}|\widetilde{p_i}\rangle\langle\widetilde{\psi_i}|r\rangle\langle r|\widetilde{\psi_j}\rangle\langle\widetilde{p_j}|\widetilde{\psi_m}\rangle \tag{3.74}$$

The charge densities $n^1(r)$ and $\widetilde{n^1}(r)$ are localized around each atom. The PAW method has been implemented in many codes such as VASP code [71, 72, 69, 70], ABINIT software [5], SOCORRO code [11] etc. This implementation has been successfully allowing the self consistent calculations of density functional theory (DFT). This method has been found to be accurate in calculation of the electronic structures.

3.2 Introduction to the VASP code

Introduction

Our calculations have been done using the VASP (Vienna ab *initio* simulation package) code [71, 72, 69, 70]. This code was written by George Kresse and Jurgen Furthmuller [71, 72] many years ago, and it has been developed at the University of Vienna in Austria by the group led by Proffesor Jurgen Hafner [69, 70].

The resources (hardware and software) required to run VASP code are very effective but commercially demanding. The operating system employed must be windows 2000/XP or Vista. The processor needed must be at least 64 bit with Opteron *AMD* or Itanium *Intel*. A more advanced one which is quad/dual Core *AMD,Intel* can perform better. At least 1 or 2 Gbytes RAM per CPU are necessary for memory requirements together with the hard drive space of 5 GB for MEDEA installation and a minimum of 60 to 300 GB for data staroge. A 17 inch monitor for visualization is sufficient but a larger one is better for graphics editing.

In order for the VASP code to operate one must be connected to the network: fast ethernet of at least 100 MBit or more is necessary. When working on a system of more than 30 atoms or on adsorption, such kinds of calculations must be submitted to cluster servers which are highly powerful and will reduce the computational cost, but for accuracy are the same as the local configurations explained above.

The developed code has been used to successfully predict the energies and properties of various solid state systems. It is based on the density functional theory method [10]. The VASP code satisfies the DFT method by its speed and accuracy. Together with the all-electron projector augmented wave potentials [19], VASP offers the accuracy

of the all-electron method while maintaining the speed and advantages of a plane wave method.

3.2.1 Types of calculations occurs in the VASP code

The VASP 4.6 code consists of four types of calculations i.e single point energy, structure optimization, ab *initio* molecular dynamics and MT-for elastic properties.

3.2.1.1 Single point energy

The single point energy calculates only the energy of the structure with the input geometries without relaxing any parameter. The only output interest is the structural energy. However in most cases after fully relaxing the structure we employ the single point energy to calculate the properties of the materials such as density of the states (DOS) and band structures. Since the single point energy converges quickly, sometimes we perform it to test the K-points and the plane wave cut-off convergence.

3.2.1.2 Structure optimization

Structure optimization is also known as geometry optimization which is concerned with relaxing the cell parameters, with or without the cell constraints. This optimization is performed at the temperature of 0 Kelvin. The said optimization is based on the three options, i.e relaxing atom positions, allowing cell shape and cell volume to change. When relaxing atomic positions, atoms are allowed to move until the residual forces between any atoms are smaller than the convergence in $eV/\mathring{A}$.

The relax atom positions can be considered alone when relaxing a surface, adsorbing a molecule on a surface and relaxing a structure around a vacancy/defect. The cell volume is allowed to change by varying the volume in keeping constant the ratios of a:b:c without changing the cell angles. This option is normally applicable alone when the pressure is applied to the system. The cell shape is allowed to change by varying

the ratio a:b:c of the lattice constants and altering the angles. The three options can be employed together in the case of fully optimizing the structure which yields the ground state's total energy and the equillibrium lattice parameters of the systems.

3.2.2 Types of properties occurs in the VASP code

In order to compute the properties of materials such as the energies, forces, band structures, densities of states, etc accurately, we need to integrate over all the occupied electron states. The computational cost increases linearly with the number of momentum space sampling points (k-points) in the Brillouin zone. DFT codes such as VASP [71, 72, 69, 70] and CASTEP [88] can approximate the k-spacing integrals with a finite sampling number of k-points. The special k-points scheme have been developed to use the fewest possible k-points to yield accurate results, thereby reducing the computational cost. The most commonly used scheme is that of Monkhorst and Pack [81] which generates efficient and accurate sets of special points in the Brillouin zone. The number of momentum k-points used mostly depends on the system as the treatment of metals, semimetals and insulators is different.

The VASP 4.6 code is able to calculate the following properties: the charge density, band structure, total local potential, density of states (DOS), electron localization function, work function and the wavefunctions of the systems. In this work, the focus is on the charge density, band structure and the density of states (DOS). These properties were calculated in two independent steps. The first step is to relax the structure and then reload the relaxed structure to calculate the properties using single point energy type of calculation.

The DOS of a system enables us to understand the number of states at each energy level that are available to be occupied by the electrons. If the DOS at the specific

energy is high, it means there are many states to be occupied. The DOS of a system is generally calculated by the equation (3.75) given below,

$$g(E) = \frac{1}{V}\frac{dN}{dE}. \tag{3.75}$$

V is the volume of the system and N is the number of electrons in it. The electronic band structure of the material describes the range of energy that an electron is forbidden, or allowed, to have [6]. This is possible due to the diffraction of the quantum mechanics electron waves in the system. The band structure enables us to understand the electronic and optical properties of the materials. The allowed energies for the electrons also depend on the wavevector (k) [6]. The wavevector k takes on values within the Brillouin zone corresponding to the crystal lattice. The points in the Brillouin zone are assigned according to the conventional name. A band structure is shown as a plot of electronic energies E(k) as a function of the momentum k. The relation is given by the equation (3.76) below,

$$E(k) = E_0(k) + \frac{\hbar^2(k-k_0)^2}{2m} \tag{3.76}$$

where E_0 and k_0 are the energy and momentum wavevector at the origin of the Brillouin zone which is known as the gamma point.

3.2.3 Types of integration schemes which occur in the VASP code

The purpose of the integration scheme is to enable the code to clearly integrate the density of states of the material. The VASP code consists of the following schemes: Methfessel-Paxton, Fermi, Gaussian, tetrahedron and tetrahedron with Blochl correction. These integration schemes focus on the k-space in the Brillouin zone, mostly on the region that divides the conduction and valence band. Each integration scheme function well on specific group of material. The gaussian and tetrahedron schemes are

employed on the insulators and semiconductors but for metals the Methfessel-Paxton is employable.

4

Results and discussion

4.1 Convergence tests of carbon and silicon structures.

Before any calculations such as electronic properties, geometry optimisation, etc, can commence, it is advisable to check the convergence of the system by calculating the total energy versus cut-off energy and total energy versus number of momentum k-points for the plane wave expansion of the wavefunction. Different cut-off energies have been tested for both carbon and silicon. The cut-off energies of 850 eV for carbon and 450 eV for silicon were found to be suitable.

Higher cut-off energies give minimum energies lower than that given by 850 eV and 450 eV: however the differences are very small (less than 1meV) and do not affect the accuracy of the results. We chose these cut-off energies to reduce computational cost. For the carbon atom, the $2p$ orbital is strongly localized because of the lack of a p core state. A large number of plane waves is required to achieve a high degree of accuracy. We observe that the cut-off energy for carbon is almost double that for silicon. In the case of silicon carbide we employed 850 eV in order to accommodate the carbon atoms.

The k-points are set according to the Monkhorst Pack scheme [81]. A 10x10x10

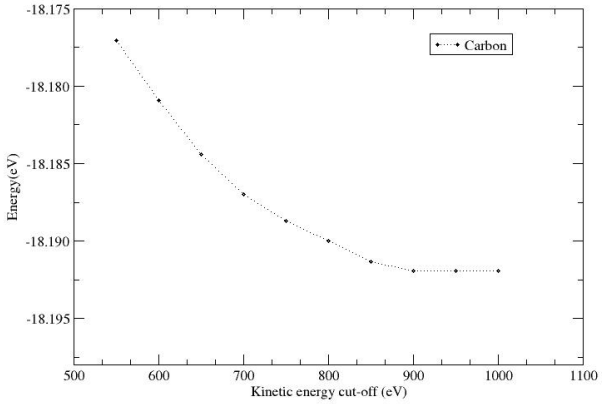

Figure 4.1: The convergence of computed total energies of carbon as a function of cut-off energy.

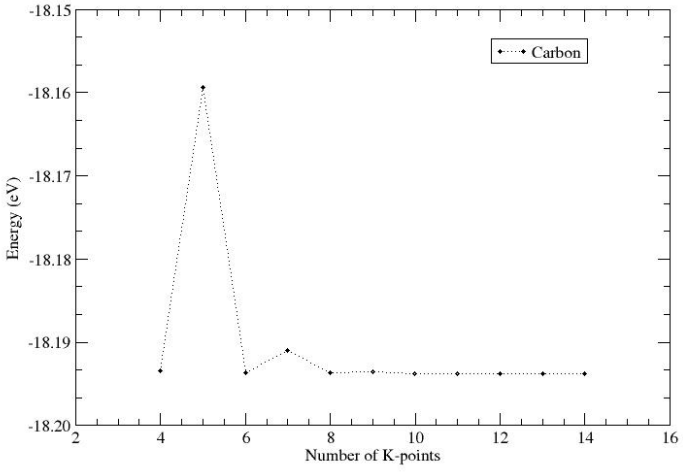

Figure 4.2: The convergence of computed total energies of carbon as a function of k-points.

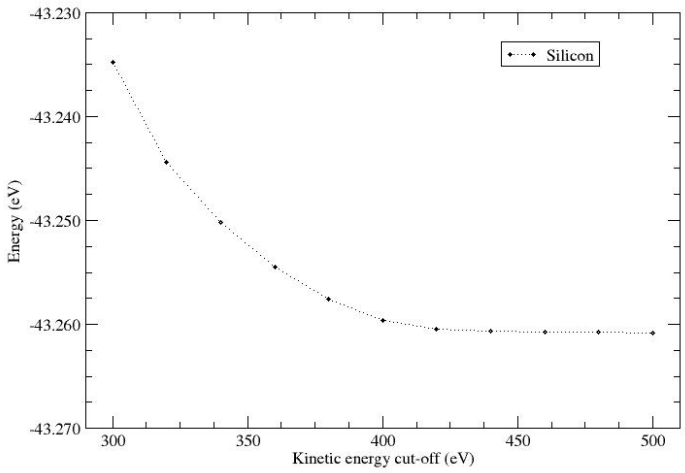

Figure 4.3: The convergence of computed total energies of silicon as a function of cut-off energy.

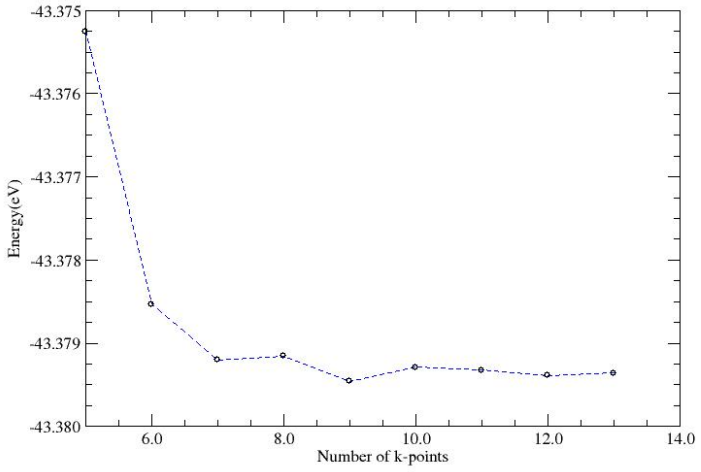

Figure 4.4: The convergence of computed total energies of silicon as a function of K-points.

mesh was used for both carbon and silicon, since it gives good convergence at a reasonable computational cost. The exchange correlation potential used in this work is the generalized gradient approximation(GGA) with projected augmented wave (PAW) pseudopotentials. The generalised gradient approximation (GGA) tends to overestimate the electronic properties i.e band gaps, but yields good cohesive energies and overestimates the lattice constants. We performed geometry optimization to fully relax the atom positions, cell volumes and cell angles of the systems. For adsorption calculations, we relax the atomic position. For electronic properties, we took the relaxed structure and perform the single point energy calculations.

4.2 Carbon, silicon in the diamond structure and SiC in the zincblende structure

In this section we investigate the structural and electronic properties of the following cubic structures, namely carbon in the diamond structure, silicon in the diamond structure and SiC in the zincblende structure. Consideration was given to the stability of the structures.

4.2.1 Structural properties

When calculating the properties of the materials, it is important to ensure that the system is in equilibrium. One way to do this is to minimize the energy and calculate the equilibrium parameters of the system that corresponds to the minimum energy. A large number of algorithms are available for energy minimization which are classified according to the order of the derivative of the total energy function employed in the calculation. The structures were minimized using the geometry optimization option found in the VASP code.

The total energy of the systems was calculated by self-consistent total energy methods.

The equilibrium lattice constants (a_0), equilibrium volume (V_o), the bulk modulus (B_o) and the pressure derivative of the bulk modulus (B_0') were calculated by fitting the energy versus volume data to the Birch Murnaghan equation of state [18] given by the equation (4.1):

$$E(V) = -\frac{9}{16}B_0[(4 - B')\frac{V_0^3}{V^2} - (14 - 3B_0')\frac{V^{7/3}}{V^{4/3}} + (16 - 3B_0')\frac{V_0^5/3}{V^2/3}] + E_0. \qquad (4.1)$$

Energies as a function of volume for carbon, silicon in the diamond structure and silicon carbide in the zincblende structure are shown in figures 4.5, 4.6 and 4.7. The parameters derived from the Birch Murnaghan equation of state [18] are listed in the table on page 69, combined with the results from other calculated works and experimental data. The minimum point on the curve corresponds to the equilibrium volume of the unit cell which gives us the equilibrium lattice parameter.

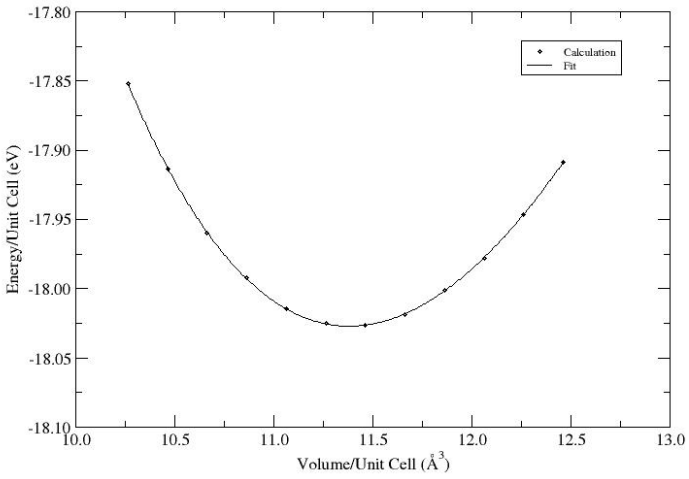

Figure 4.5: The total energy versus lattice parameter of carbon in the diamond structure.

Our calculated equilibrium lattice constant for carbon in the diamond structure was found to be 0.28% greater than the result reported by Chang et al. [28] employing

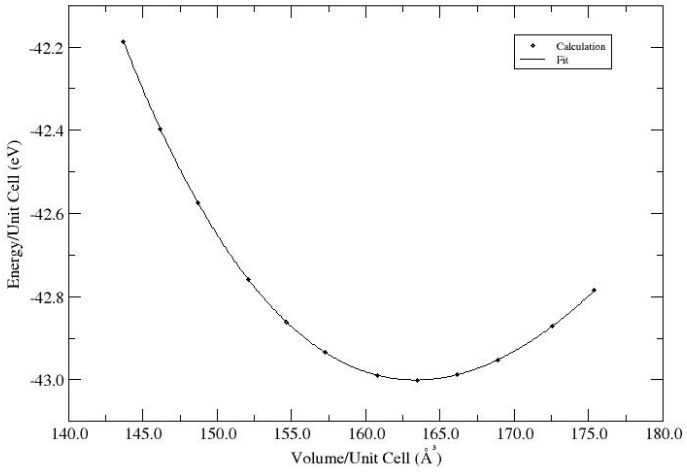

Figure 4.6: The total energy versus lattice parameter of silicon in the diamond structure.

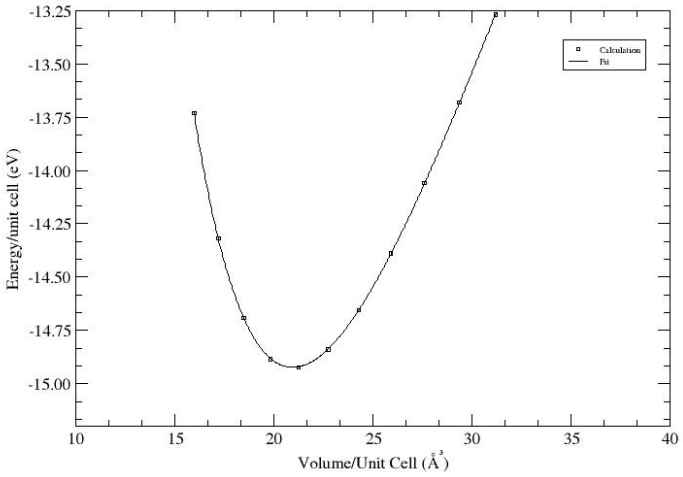

Figure 4.7: The total energy versus lattice parameter of SiC in the zincblende structure.

LDA [57] and 0.112% greater than the experimental result. We observe that our calculated equilibrium lattice constant is closer to the experimental value when compared to the work reported by Chang et al. [28]. Our calculated bulk modulus was found to be 2.257% less than the experimental bulk modulus and 1.14% less than that done by Chang et al. The use of GGA underestimates the bulk modulus compared to the use of LDA. Our calculated bond length was found to be 3.870% less than the calculated work reported by Chang et al. [28] and 4.54% less than the experimental value. The overall results show that carbon in the diamond structure is a stiff (hard) material.

In the case of silicon in the diamond structure, our calculated equilibrium lattice constant was found to be 0.626% more than the value calculated by Ying et al. [116]. When compared to the experimental work, our value was found to be 0.699% more. This shows that our calculation employing GGA is an improvement over the value calculated by Ying et al. [116]. We observe that silicon has a greater lattice constant compared to carbon. This is caused by the excess of p core states in the silicon atom having large atomic radius than carbon atom. Our calculation for the bulk modulus is 3.52% less than the calculated work reported by Ying et al. [116] and 10% less than the experimental value. Our calculated bond distance was found to be 1.73% more than the work done by Ying et al. [116] and 0.08% more than the experimental work. This long bond length is responsible for the underestimation of bulk modulus which reveal that silicon in the diamond structure is not as stiff (hard) as carbon.

In our calculations for SiC in the zincblende structure, our lattice parameter was found to be 4.38$\mathring{A}$, which is 0.45% more than in the work of Chang et al [28] and the experimental data. Our calculated lattice constant was found to be more than that of carbon but less than that of silicon. The calculated bond length was found to be 0.2% less than the experimental data. The calculated bulk modulus was found to be 6% less

than the experimental data and 1.5% less than the value reported by Chang et al. [28]. Our results reveal that SiC the zincblende structure falls under Hard material.

4.2.2 Cohesive energies

The cohesive energies were calculated as the energy difference between the total energy of the free atoms and the bulk solid as given by the equation below:

$$E_{coh} = E_{atom} - E_{solid}. \tag{4.2}$$

The table on page 69 shows that our calculated cohesive energy for carbon in the diamond structure is 3% less than that calculated by Chang et al. [28] employing LDA. This demonstrates the overbinding of the LDA compared to GGA. Our calculated cohesive energy using GGA is higher than the experimental work. Our result indicates a lesser overbinding when compared to the one calculated by Chang et al. [28]. In the case of silicon in the diamond structure, our calculated cohesive energy was found to be 0.4% less than that reported by Ying et al. [116]. Even in this case we observe the greater overbinding of the calculated results when using LDA rather than GGA. Our calculated cohesive energy was found to be equal to experimental data. These kinds of result indicate that GGA is the better exchange correlation to use when approximating the cohesive energies of the materials. In the case of SiC in the zincblende structure, our calculated cohesive energy is clearly comparable with both LDA and experimental data. Even in this case, we observe that our calculated result using GGA is closer to the experimental data with a percentage difference of 0.3%.

Table 4.1: The calculated and experimental equilibrium lattice constants (a_0), equilibrium bond distances (bd), equilibrium volumes (V_0), cohesive energies(E_{coh}), bulk moduli(B_0), bulk moduli prime B_0'. Letter C refers to [28], F to [37], [79], [22], G to [77], H to [115],I to [111],B to [117]

This work	structure	space group	a_0 (Å)	bd(Å)	$V_0(\mathring{A}^3)$	$E_{coh}(eV)$	$B_0(GPA)$	B_0'
	Carbon in diamond	Fd-3m	3.571	1.545	45.530	7.700	43.300	4.010
	Silicon in diamond	Fd-3m	5.467	2.350	163.360	4.630	88.740	4.270
	SiC in zincblended	Fd-3m	4.376	1.900	83.820	12.720	208.760	3.990
Other work								
	Carbon in diamond	Fd-3m	3.560^c	1.551	45.160^c	7.940^c	43.800^c	3.500^c
	Silicon in diamond	Fd-3m	5.430^d	2.310	160.370^d	4.850^d	92.000^d	3.600^c
	SiC in zincblended	Fd-3m	4.360^c	1.896^c	82.940^c	13.320^c	212.00^c	3.700^c
Experimental								
	Carbon in diamond	Fd-3m	3.567^F	1.540	45.390^F	7.370^F	44.300^F	4.000^F
	Silicon in diamond	Fd-3m	5.429^B	2.352	160.010^B	4.630^B	99.000^B	4.200^B
	SiC in zincblended	Fd-3m	4.360^G	1.890	82.880^G	12.680^H	224.000^I	

4.2.3 Electronic properties

In this section, we calculated the electronic properties of carbon, sillicon in the diamond structure and SiC in the zincblende structure. The fully relaxed structures were used to evaluate the electronic properties.

4.2.3.1 Density of states

The total density of states for carbon and silicon in diamond structure and SiCin zincblende structure is depicted in figures 4.8, 4.9 and 4.10 respectively. We observe that in all cases, the conduction and valence bands are separated by energy band gaps.

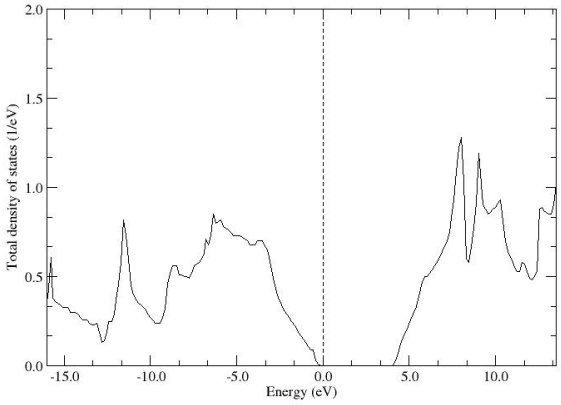

Figure 4.8: The total density of states for carbon in the diamond structure.

The figure 4.8 indicates the plot of the total density of states for carbon in the diamond structure. It shows a wide band gap of $4.31eV$ which is less than the experimental value of $5.46eV$ measurements which Clark et al. [31] observed using neutron diffraction. Our calculated band gap shows an improvement when compared to the $4.0eV$ calculated by Ruedi et al. [23] using EHMO-ASED [98]. This kind of band gap is predicted by sp^3 type of bonding which suggests that the structure is an insulator. Considering the electronic contributions from lower to higher energy we discuss the

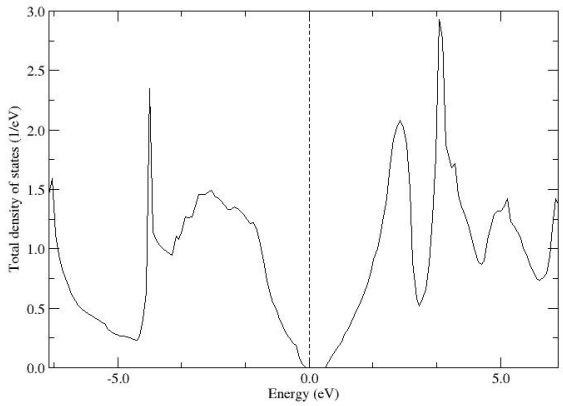

Figure 4.9: The total density of states for silicon in the diamond structure.

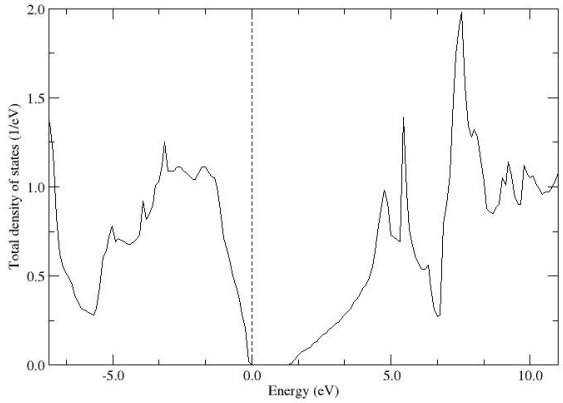

Figure 4.10: The total density of states for SiC in the zincblende structure.

peaks as follows: we observe the sharp peak at $-12eV$ which indicates the (σ) bond at the valence band. At $-5eV$ we observe the highest peak even though it is not the sharpest peak, which suggest that the highest states are fully occupied but the bonding is still (σ). We observe the reduction of the density of states towards the Fermi level until $0eV$ where the density of states varnishes completely.

Figure 4.9 gives the total density of states for silicon in the diamond structure with a small band gap of $0.579eV$. Our calculated band gap is less than the experimental value of $1.12eV$ reported by [107]. Our calculated band gap shows an improvement compared to the value of $0.52eV$ calculated by Cohen et al. [32] using LDA. This indicates that GGA tends to improve the band gap predicted by LDA but is still less that the experimental value. This size of the band gap gives a clear indication that silicon in the diamond structure is a semiconductor material.

Considering the electronic contributions from lower to higher energy we discuss the peaks as follows: At the energy of $-6.5eV$, we observe the sharp peak which mainly possesses an electrons of s orbital character. This peak indicates a higher density of states compared to the region of $-4eV$ which have less electrons contribution. At $-2eV$ we observe the two high peaks which mainly consists more electrons contribution of p orbital. Beyond $-2eV$, we observe a reduction of density of states until to 0 eV (Fermi energy) where the electrons contribution vanishes completely.

Figure 4.9 depicts the total density of states for silicon carbide in the zincblende structure with a band gap of $1.530eV$. Our calculated band gap is better than the band gap of $1.37eV$ calculated by Karch et al. [62] employing (LDA). Our calculated band gap is still lower than the experimental value of $2.39eV$ found by Madelung et al. [77]. This band gap shows that SiC in the zincblende structure is a semiconductor material. Considering the electronic contributions from lower to higher energies, we discuss the peaks of different energies (positions). Our calculated peak positions of $-3.0, -5.0, -8.0$

and $-12.0eV$ compare well with the experimental values $-3.0, -5.0, -8.5$ and $-12.8eV$ obtained using soft x-ray valence spectrums, reported by G. Wiech [113]. They also compare well with the calculated work done by K. Karch et al. [62] employing LDA.

We observe the highest sharp peak at $-8.0eV$ formed by the contribution of electron of s orbitals for the carbon and silicon atoms. This peak reveals that there are more electrons contribution compared to other regions. At $-3.0eV$, there exists a rough peak which indicates the contribution of electrons of p orbitals for both silicon and carbon atoms. This peak shows the less electrons contribution comparared to the previous one. The bonding occurring in silicon carbide is polar covalent whereby silicon acts as a cation and carbon as anion.

4.2.4 Discussion

The lattice constant of carbon in the diamond structure was found to be much less than that of silicon and silicon carbide (SiC). This is due to the deep pseudopotentials of carbon particularly in the p state. Our calculated errors to experimental values were found to be within the acceptable range of DFT. The lattice constant of SiC in the zincblende is smaller by $0.143\mathring{A}$ than the geometric average of the lattice constants for silicon and carbon. This reduction of the lattice constant is stated clearly in alloy theory and is known as Vegard's rule [35]. This is caused by the charge transfers from the silicon atom to the carbon atom, due to the strong $2p$ potential of carbon. We observe that our calculated cohesive energy for SiC is larger than the geometric average of silicon and carbon. We conclude that SiC in the zincblende structure is thermodynamically stable.

4.3 Carbon, silicon and silicon carbide in the graphene structure

In this section three types of graphene related structures namely: two dimensional carbon, silicon and silicon carbide honeycomb are investigated. The carbon and silicon in the graphene structure are already experimentally existing [84, 40] while silicon carbide in this structure has not been synthesised but is a possible structure. All our structures contain two atoms basis in the 1x1 primitive unit cell.

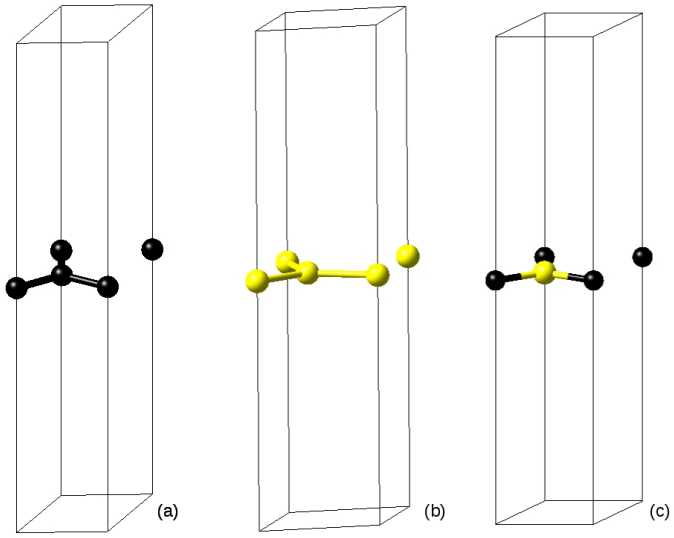

Figure 4.11: The (1x1) unit cells of two dimensional graphene structures (a) carbon in the graphene structure, (b) silicon in the graphene structure and (c) silicon carbide in the graphene structure.

4.3.1 Structural properties

We calculated the structural and electronic properties of C, Si and SiC in the graphene structures employing geometric optimization. Carbon in the graphene structure is planar in all geometric arrangements with the lattice vectors $a = b = 2.47\mathring{A}$ and $c = 15\mathring{A}$. The lattice vector c was set large enough in order to avoid interlayer-spacing interactions. The calculated total energies in relation to lattice constants are shown in

figures 4.12, 4.13 and 4.14. The minimum points on each curve indicate the equilibrium lattice constant at the ground state total energy. Our calculated parameters and cohesive energies are summarized in the table 4.2. There are no experimental results for SiC in the graphene structure but there are results from previous work to validate our results [15].

Our calculated lattice constant for carbon in the graphene structure was found to be 0.5% more than the experimental data and the result reported by [15]. The corresponding bond length was found to be 0.42% more than the experimental bond length. Our estimated structural parameters for carbon in the graphene structure relative to experimental data are within acceptable limits. The structure of carbon in the graphene structure is predicted to be planar because of the formation of a π bond between the two nearest neighbour carbon atoms. The strong covalent σ bond from sp^2 hybridization between adjacent carbon atoms is also responsible for the planar geometry. This also causes the unusual electronic properties of carbon in the graphene structure.

Table 4.2: The calculated and experimental equilibrium lattice constants (a_0), equ ilibrium bond distances (bd) and cohesive energies(E_{coh}). All data of other work are from reference [15], experimental data for carbon in the graphene structure and silicon in the graphene are from references [84],[40]

This work	structure	space group	$a_0(\AA)$	$bd(\AA)$	$E_{coh}(eV)$
	Carbon in graphene	P6/mmm	2.471	1.426	8.730
	Silicon in graphene	P6/mmm	3.848	2.222	4.330
	SiC in graphene	P6/mmm	3.096	1.787	13.140
Other work					
	Carbon in graphene	P6/mmm	2.465	1.420	10.400
	Silicon in graphene	P6/mmm	3.830	2.200	4.900
	SiC in graphene	P6/mmm	3.070	1.770	15.250
Experimental					
	Carbon in graphene	P6/mmm	2.46	1.420	7.600
	Silicon in graphene	P6/mmm	3.900	2.240	....
	SiC in graphene	P6/mmm	....	....	....

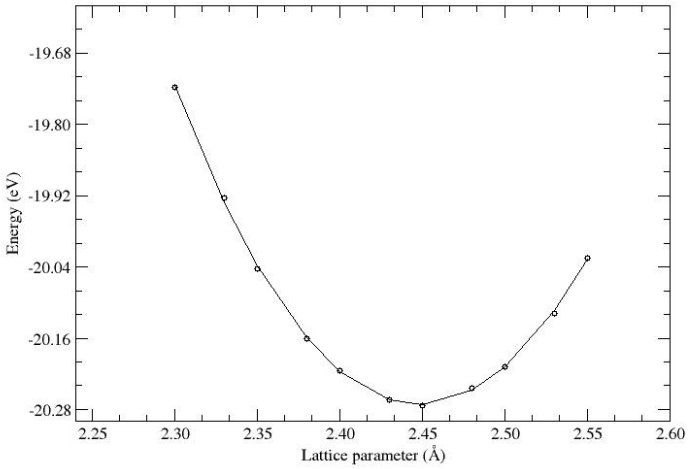

Figure 4.12: The total energy versus lattice parameter of carbon in the graphene structure.

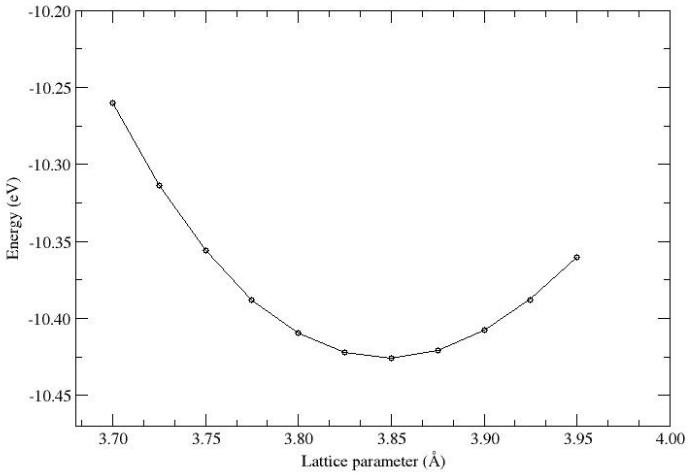

Figure 4.13: The total energy versus lattice parameter of silicon in the graphene structure.

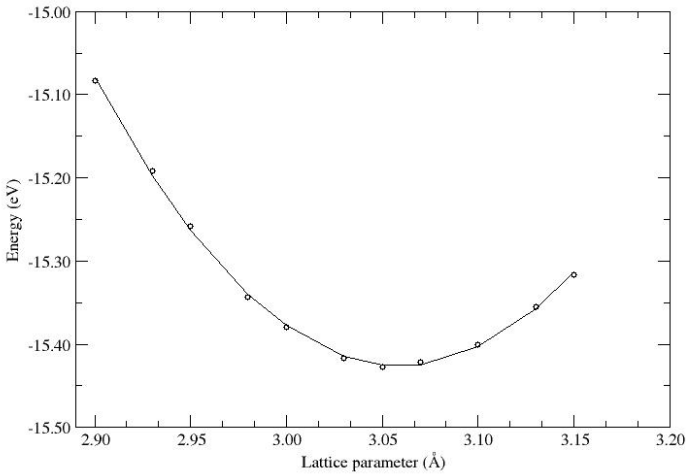

Figure 4.14: The total energy versus lattice parameter of silicon carbide in the graphene structure.

In the case of silicon in the graphene structure, we observe a lattice constant of 0.77% lower than the experimental data [40]. This underestimated lattice constant is a surprising result since we are aware that GGA tends to overestimate the experimental lattice constants. We notice that our underestimated value is still within the acceptable limits. However our calculated lattice constant shows an improvement compared to the other calculated values employing LDA. Our calculated bond length of $2.222\mathring{A}$ is clearly comparable with the experimental result of $2.240\mathring{A}$ and the calculated result of $2.200\mathring{A}$ done by Kara et al. [39]. Because silicon in the graphene structure is two dimensional, we expect it to behave like carbon in the graphene structure since kara et al. [39] reported that its charge carriers are also massless relativistic Dirac fermions. The structure also appears to be two dimensional with a strong σ bond between two adjacent silicon atoms. There also exists π bonding between silicon atoms. This π bonds are responsible for the structure being semimetallic with unusual electronic properties. This is revealed by the calculations of electronic properties.

In the case of SiC in the graphene structure, our calculated lattice constant appear to be 0.85% more than the calculated results reported from reference [15] while our calculated bond length appears to be 1% more. In all systems, the percentage errors are within the computational acceptable limits. We compared our parameters with the results performed using LDA calculations employing ultrasoft pseudopotentials. The interesting part is that our calculations perform better than those done using LDA.

We further tested the stability of the structure by displacing the atoms $0.5\mathring{A}$ away from their original positions and allowing the structure to fully relax. After relaxation, all atoms returned to their original positions and the layer remained flat (planar). This observation implies that the structure is stable with one ground state. We continued by further investigating the stability of SiC: calculating the density of states (DOS) and analyzing the peaks. In the case of SiC in the graphene structure, we observe the reduction of the lattice constant for carbon, which implies that the volume of the unit cell of silicon carbide is smaller than that of carbon in the graphene structure but greater than that of silicon in the graphene structure.

4.3.2 Cohesive energy

Cohesive energies were calculated by taking the energy difference between the equilibrium energy of the atoms in the graphene structure and the energy of the independent atoms stated from (4.2). Our calculated cohesive energy for carbon in the graphene structure was found to be 12.98% more than the experimental value, which shows overbinding in the exchange correlation used. However, our calculated cohesive energy indicates less overbinding compared to the other calculated results reported by [15] employing the local density approximation. These results show an overbinding of 36.842% more than the experimental results. In the case of silicon and SiC in the graphene

structure there are only theoretical results to compare with ours. Our calculated cohesive energy shows an underestimation compared to other calculated results [15].

4.3.3 Density of states

Electronic properties were calculated at an equilibrium (ground state) structure employing single point energy calculations. We give a brief description of the electronic behaviour of three structures. In these calculations, the electronic states were occupied in accordance with the Fermi distribution function with a Fermi smearing parameter of $k_BT = 0.2eV$. We choose 18x18x1 for the Monkhorst-Pack grid. This is considered to be a high density of sampling for integrating in the Brillouin zone which we employ to minimize numerical errors.

The corresponding densities of states for carbon, silicon and SiC in the graphene structures are shown in figures 4.15, 4.16 and 4.17 respectively. Figure 4.15 gives the total density of states for carbon in the graphene structure. We notice that the DOS plot gives no band gap between conduction and valence bands (no band gap but also no overlap between conduction and valence band) at the Fermi energy. This property was also revealed by Wallace et al. [112]. This absence of band gap is caused by the joining of conduction and valence bands at the bottom of the Fermi energy at the Γ-point of the Brillouin zone. Theoretically, a zero band gap reveals that carbon in the graphene structure is semimetallic.

We observe the first long peak located at an energy of $-14eV$ of an s orbital character. This is essential for non-bonding orbitals at the core states. We also observe peaks ranging from -4 to $-7eV$ for $2sp^2$ hybridization states with the p_z orbital perpendicular to the plane. The electrons at these states are energetically active and are capable of providing the upper bound for the valence band. However the p_z orbital is

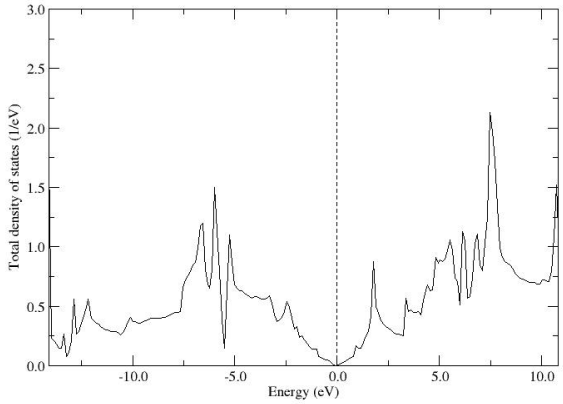

Figure 4.15: The total density of states for carbon in the graphene structure.

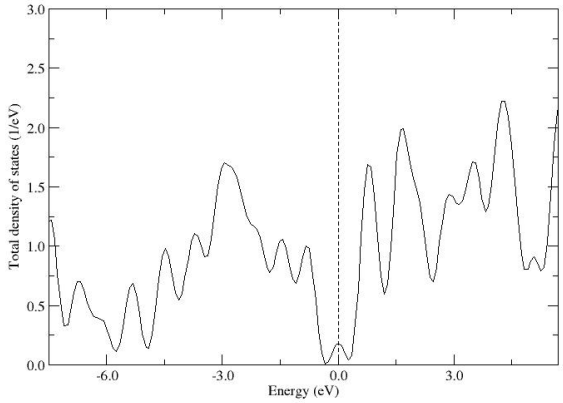

Figure 4.16: The total density of states for silicon in the graphene structure.

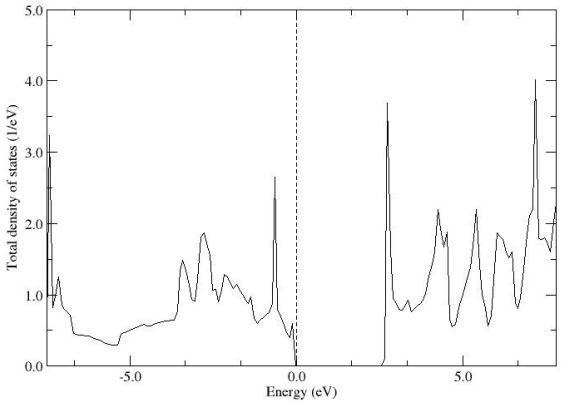

Figure 4.17: The total density of states for silicon carbide (SiC) in the graphene structure.

responsible for the joining of the conduction and valence band energies at the bottom of Fermi energy. The figure 4.15 shows a conical (linear) dispersion with respect to the Γ-point. This reveals that the bands contain massless Dirac Fermion states.

The plot of the density of states (DOS) for silicon in the graphene structure indicates no band gap at the Fermi energy. This behaviour was also observed by Ciraci et al. [15], which indicates that the bands cross the bottom of the Fermi level at the corners of the Brillouin zone. This also reveals that silicon in the graphene structure is semimetallic. The peaks range from -2 to $-4eV$, showing that electrons for the $2sp^2$ hybridization states are energetically excited and there is strong σ bonding between the Si atoms. These peaks are caused by the electronic contribution of p_z orbitals which is perpendicular to the plane and is responsible for π bondings (bands). These π bondings are weak and cross at the bottom of the Fermi level. We observe a flat reduction of the electronic states from -1 to $0eV$ (Fermi) energy. Comparing the peaks for silicon in the graphene structure with that of carbon in the graphene structure, we observe a higher peak of 2.0 states/eV in the silicon graphene structure. This peak

is 0.5 states/eV more than that of carbon in the graphene structure. This might be due to the fact that carbon makes a lesser electronic contribution than silicon in the p orbital. Theoretically, the long peak shows more electrons contribution, which reveals that silicon in the graphene structure is less stable than carbon in the same structure.

Figure 4.17 depicts the total density of states (DOS) for silicon carbide (SiC) in the graphene structure. We observe that the valence and conduction bands are separated by a wide band gap of $2.542eV$. This band gap indicate that SiC in the graphene structure is a semiconducting material. We observe the highest peak of 1.5 states/eV at an energy of $0.30eV$. This peak is due to the contribution of electrons for $2sp^2$ hybridization. Even in this structure, the bonding occurring between the atoms is covalent with the electron moving from silicon to carbon atoms.

Comparing the peaks of the three structures, we observe that carbon in the graphene has the lowest peak. Careful analysis of the SiC structure shows that the peak is just slightly higher than that of carbon in graphene. This indicates that SiC in the graphene structure is less stable than carbon in the graphene structure. Our results for SiC in the graphene structure indicate that it is a plausible structure.

4.4 Carbon, silicon and silicon carbide in the graphane structure

4.4.1 Adsorption of a single hydrogen atom and a pair on carbon in the graphene structure

In this section, the adsorption of single and pairs of hydrogen adatoms on different sizes of supercells of carbon in the graphene structure, i.e (1x1), (2x2), (3x3) and (4x4) is considered. We started by employing the (1x1) unit cell for the adsorption of a hydrogen

adatom to establish the most favourable site between the ontop and hollow sites. Our calculations reveal that the hydrogen adatom prefers to be adsorbed on the ontop site. The minimum energy for the hollow site adsorption was found to be $0.323eV$ more than the ontop site adsorption. Our calculated bond distance between carbon and hydrogen was found to be $0.043\mathring{A}$ less than the distance between the hollow site and hydrogen adatom. This revealed to us that the ontop site adsorption displays stronger bonding than the hollow site. For the other supercell sizes, we adsorbed hydrogen adatoms on the ontop site.

We continued to investigate whether a pair of hydrogen adatoms prefer to be adsorbed on the same side or alternating sides. The minimum energy for alternating adsorbed hydrogen adatoms was found to be $1.877eV$ less than the minimum energy for hydrogen adatoms adsorbed on the same side. Our calculated bond distance between carbon and hydrogen atoms for the alternating case was found to be $1.102\mathring{A}$ symmetric for both hydrogen adatoms. For hydrogen adatoms adsorbed at the same side, their distance from the layer was found to be $1.110\mathring{A}$ symmetric. For both situations, we applied different configurations, including placing the hydrogen adatoms assymetrically and moving them slightly along the xy direction. However, after relaxation both two hydrogen adatoms remained symmetric on top of carbon atoms. Therefore our calculations reveal that the hydrogen adatoms prefer the alternating adsorption case. We decided to consider various configurations on the other supercells by adsorbing the hydrogen adatoms on the same side in order to be able to make a comparison with the work on adsorption of lithium adatoms and to include the effect of the force of repulsion between hydrogen adatoms on the same side.

Our calculated geometric parameters and binding energies are summarized in the table on page 85. Our calculated results compare well with the other calculated data

and in most cases show an improvement. This suggests that GGA is a better exchange correlation to use than the LDA. Our results were strongly affected by the sizes of the unit cells and imply that (3x3) and (4x4) supercells have better degrees of freedom than the others. This also suggests that, for (1x1) unit cells, there are high interactions (repulsion) between hydrogen atoms due to symmetry operations whereas for a (4x4) supercell, the hydrogen atom is in an isolated state where the interactions are minimal. For our calculations of electronic properties we employed the (4x4) unit cell.

Our binding energies were calculated as follows:

$$E_{bind} = E_{HC} - E_H - E_C \tag{4.3}$$

where E_{HC} is the energy per hydrogen adatom of the carbon in the graphene unit cell, E_H is the total energy of an isolated hydrogen adatom and E_C is the energy of pristine graphene unit cell. Our calculated binding energies are greatly affected by the increase in the supercell sizes and were in agreement with the other calculated results. We observe that the binding energy for single hydrogen adsorption on a (4x4) unit cell is $0.948eV$, which is in agreement with the $0.890eV$ result in Denis et al. [34]. For pairing of hydrogen adatoms, we considered five pairs which are illustrated by figure 4.18 and labelled as P_1, P_2, P_3, P_4 and P_5. Our calculated binding energies show that the odd pairs are energetically more favourable than the even pairs. The binding energies for odd pairs appear to be greater than those of the two isolated adsorbed atoms; however these pairs are regarded as the stable ones. This suggests that the odd pair are in a good position as regards the hydrogenation process. But this does not mean the even pairs fail: they may but will require a high amount of energy. When considering odd pairs, we discovered that stability decreases with the increase of the H-H separation. We can conclude that P_1 is the most stable configuration which is in agreement with

Table 4.3: The calculated and experimental equilibrium height d_{puck} ($\mathring{A}$), carbon-carbon [C-C ($\mathring{A}$)] distance and hydrogen-carbon [H-C $\mathring{A}$] coresponding to different sizes of supercells. Letter c refers to reference [96], a refers [34], b refers to [101] and d refers to [63]

	This work				Other works			
Geometric Parameters	Bond distances				Bond distances			
Single H adatoms	1x1	2x2	3x3	4x4	1x1	2x2	3x3	4x4
$d(H-C)$	1.181	1.126	1.130	1.128	1.121^a	...	...	1.138^a
$d(C-C)$	1.482	1.476	1.476	1.478	...	...	...	1.496^a
d_{puck}	0.299	0.465	0.465	0.492	0.490^a	0.360^b	0.410^d	0.481^a
Pair of H adatoms								
$d(H-C)$	1.110	1.118	1.127	1.124				
$d(C-C)$	1.486	1.485	1.484	1.486	...	...	...	1.512^a
d_{puck}	0.458	0.458	0.472	0.532	...	...	...	0.710^a
Configurations	Binding energies				Binding energies			
	1x1	2x2	3x3	4x4	1x1	2x2	3x3	4x4
P_1	1.89	1.823	1.834	1.845	...	...	...	1.800^c
P_2	...	0.360	0.427	0.789	...	...	...	0.600^c
P_3	...	1.890	1.147	1.497	...	...	...	1.200^c
P_4	...	0.611	0.349	0.784	...	...	...	0.650^c
P_5	...	1.370	1.137	1.245	...	...	...	...
Single	0.435	0.659	0.855	0.948	0.560^a	0.670^a	0.760^a	0.850^a

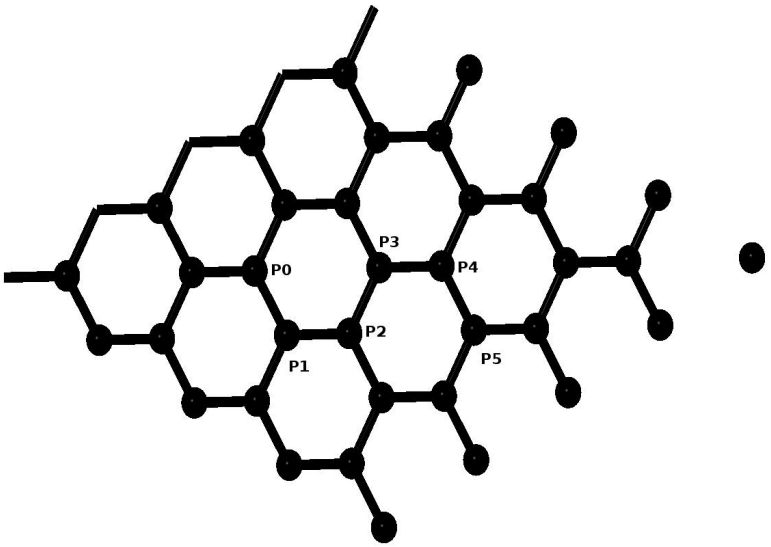

Figure 4.18: Structure of carbon in the graphene structure for a (4x4) supercell. The letters P0 indicate the position where a single hydrogen adatom was adsorbed and is the first hydrogen to be paired with others. P1 to P5 is the route used for pairing with P0.

the work done by Roman et al. [96]. This reveals that the hydrogen-hydrogen interactions are also responsible for stabilising the structure. The (2x2) supercell indicates that P_3 is also the most stable configuration but we doubt the size of the cell for the hydrogenation process. Our calculated binding energies for the higher concentration indicate greater stability, which makes carbon in the graphene structure a candidate for hydrogen storage.

In this paragraph the geometrical properties of the most stable configuration (P_1) for different supercells only are discussed. The binding energies discussed above are correlated clearly with the geometric parameters. These parameters were found after the addition of hydrogen adatoms on top of the carbon in the graphene sheet. For a (1x1) unit cell after adsorption of single hydrogen adatoms, we observe the depuckering height of $0.299\mathring{A}$ which increases to $0.458\mathring{A}$ when hydrogen adatoms are paired. This tells us that the layer is no longer flat but buckled. The calculated H-C distance for single hydrogen was found to be $1.181\mathring{A}$ for a (1x1) cell but decreased when the supercell is increased. The adsorption of single hydrogen adatom breaks the double bond and releases unpaired electron. This requires us to adsorb the second hydrogen adatom so that all bonds are saturated. We observed the decrease of H-C bond distances when the second hydrogen adatom is adsorbed.

The two hydrogen adatoms pairs appear to be symmetrical after relaxation. This symmetric behaviour tells us that if the hydrogen adatoms can be clustered, they can form a flat layer on top of buckled carbon atoms in the graphene layer. We observe that this H-C bonding is also affected by this greater size of the cell. We observe that our result of C-C bonding for single hydrogen adatom was not affected by this size of the unit cells, but was only affected by the addition of the second hydrogen adatom. Our calculated C-C bonding results are found to be greater than the value of pure graphene

of 1.426$\mathring{A}$, which reveals that there exists a transformation of the sp^2 hybridization in the pristine carbon located in the graphene structure, to sp^3 hybridization in the hydrogenated carbon graphene. Our calculated value is still less than the 1.540$\mathring{A}$ of pure carbon in the diamond structure.

4.4.1.1 Density of states

The density of states was calculated in order to observe the electronic changes caused by the adsorption of hydrogen adatoms on top of carbon in the graphene structure. Only the DOS of the (4x4) supercell is shown since it has better stability than the others. We started with the density of states for the adsorbed single hydrogen adatoms followed by the adsorbed pair of hydrogen adatoms. We wanted to understand the effect of a single hydrogen adatom on the layer which leaves one electron of carbon unpaired and a fully saturated hydrogenated structure respectively. To obtain a self-consistent charge density we employed higher meshes of 18x18x1 for the integration over the irreducible part of the Brillouin zone.

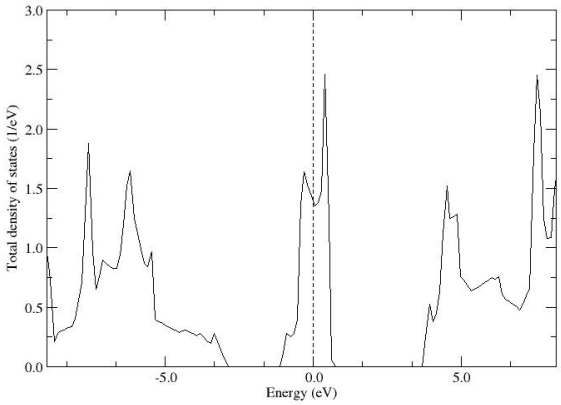

Figure 4.19: The total electronic density of states for single hydrogen adatom adsorbed on the carbon in the graphene structure.

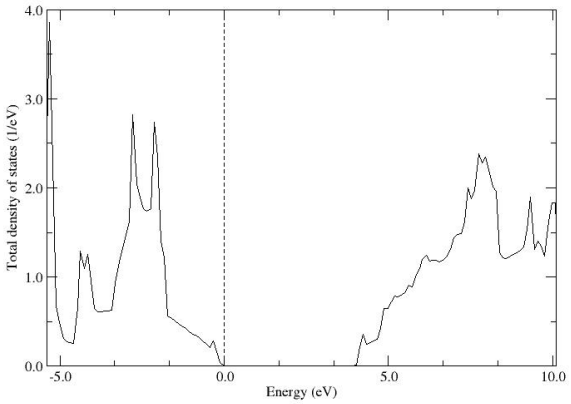

Figure 4.20: The total electronic density of states for pair of hydrogen adatoms adsorbed on the carbon in the graphene structure.

Figure 4.19 depicts the resulting density of states for single hydrogen adsorbed on the carbon in the graphene structure. We observe a great difference when compared to the DOS of pure pristine carbon in the graphene structure. A tuned gap between the valence and conduction band is observed. Furthermore, a long peak at the centre of the gap along the Fermi level is present. We claim that this long peak around the Fermi level is caused by the excess of unpaired electron. This reveals that single hydrogen adatom adsorption possesses pure metallic properties in the system. At the energy of -7 eV in the valence band we observe a peak which indicates strong bonding between the electron from s orbital of the hydrogen adatom and the electron from the p orbital of carbon atom.

Since we observed that the adsorption of a single hydrogen adatom leaves an unpaired electron on the structure, we decided to adsorb another hydrogen atom. Figure 4.20 illustrates the density of states for a hydrogen adatoms paired structure. We observe the disappearance of the long peak around the Fermi level with the valence and conduction bands being separated by a band gap of $3.965eV$. This gap is in agree-

ment with the experimental one reported by Elias et.al [38] of $3.5eV$. The said gap reveals that the adsorption of paired hydrogen adatoms transforms the structure from a semimetallic one to an insulator. The long peak at an energy of around $-3eV$ on the valence band demonstrates the contribution of sp^2 for carbon but only s for hydrogen which leads to strong sp^3 hybridization. Since the valence band is dominated by the s and p orbitals, it can be concluded that our observed insulating band gap is one of s-p type bonding.

In these calculations, several factors are suspected of being responsible for the hydrogen adatom inducing a band gap. Such defect of the buckled layer is caused by the adsorbed hydrogen adatom. We suggested this because the structure is taking a three dimensional shape. The hydrogen H^+ ionic core may be responsible for generating the gap. We decided to take the fully adsorbed structure and remove the hydrogen adatoms. We then recalculated the DOS of the buckled structure with their absence. The recalculated DOS appears the same as the one for pristine planar carbon in the graphene structure, with the absence of a band gap. We concluded that the H^+ is responsible for the generation of the large band gap and that the charge transfer from hydrogen adatoms to carbon atoms indicates covalent bonding.

4.4.2 Adsorption of single and paired hydrogen adatoms on silicon in the graphene structure

In this section, several configurations are also considered for the adsorption of hydrogen adatoms employing different sizes of supercells. We started by adsorbing a single hydrogen adatom on top of silicon and on a hollow site. After relaxation, our calculated binding energies reveal that the ontop site is lower in energy than the hollow site, by an amount of $0.4meV$. This energy difference is relatively very small, which shows that under conditions of finite temperature, islands of hollow sites may co-exist with islands

of ontop sites. This was also observed by Ryou et al. [97]for adsorption of hydrogen on silicon nanotubes.

After relaxation, the hydrogen adatom moved from the hollow site directly to the ontop site. The bond distance from the hydrogen to silicon (H-Si) for the ontop site calculation was found to be $1.522\mathring{A}$, and $1.523\mathring{A}$ for the hollow site calculation. This short bond also proves that the ontop site is the preferred site. We continued further to investigate whether a pair of hydrogen adatoms prefers to be adsorbed on the same side or alternating sides. The minimum energy for alternating adsorbed hydrogen adatoms was found to be $1.553eV$ less than the minimum energy of hydrogen adatoms adsorbed on the same side. The energy difference indicates that the alternating adsorption is more stable than the same side adsorption. As we stated earlier that this is a comparative study we continue with the adsorption of hydrogen adatoms at the same side of the silicon layer. Our calculated structural parameters and energies are summarized in the table on page 92.

The binding energies are calculated using equation (4.3) and the adsorption of hydrogen adatoms was performed following the route indicated on figure 4.21 referring to the layer of silicon adatoms in the graphene structure. In this calculation we observe that an increase in the sizes of the unit cells affects the binding energies of the system. For single hydrogen adatoms adsorption, we observe that the (4x4) supercell displays the highest binding energy compared to the small supercells. This value shows that hydrogen adatom has a good degree of freedom when interacting with silicon in the graphene structure.

The coresponding depucking distance (outward movement of silicon atom) was found to be $0.647\mathring{A}$. This value is reasonably large to indicate that the structure is

Table 4.4: The calculated equilibrium height d_{puck} ($\mathring{A}$), silicon-silicon [Si-Si ($\mathring{A}$)] distance and hydrogen-silicon [H-Si ($\mathring{A}$)] corresponding to different sizes of supercells.

Geometric Parameters	Bond distances			
Single H adatom	1x1	2x2	3x3	4x4
$d(H-Si)$	1.522	1.492	1.513	1.511
$d(Si-Si)$	2.332	2.334	2.339	2.341
d_{puck}	0.474	0.334	0.637	0.647
Pair of H adatoms				
$d(H-Si)$	1.493	1.495	1.515	1.513
$d(Si-Si)$	2.341	2.331	2.336	2.342
d_{puck}	0.492	0.456	0.779	0.848
Configurations	Binding energies			
	1x1	2x2	3x3	4x4
P_1	1.507	1.213	1.558	1.715
P_2	...	1.046	1.489	1.679
P_3	...	1.351	1.543	1.703
P_4	...	1.045	1.378	1.615
P_5	...	..	1.543	1.643
Single	0.778	0.514	0.711	0.834

no longer planar. This furthermore indicates that by adsorbing one hydrogen adatom there is a transformation from sp^2 to sp^3 hybridization. Our calculated distance between two silicon adatoms (Si-Si) was found to be $2.341\mathring{A}$. This value is greater than our calculated value of $2.222\mathring{A}$ for pristine silicon in the graphene structure. Our calculated value of $2.341\mathring{A}$ is closer to the value of silicon in the diamond structure of $2.350\mathring{A}$. When hydrogen atoms were paired we still observe that the (4x4) supercell is more stable than the others.

In terms of binding energies, we observe that the odd pairs (P1,P3,P5) bind better than the even pairs (P2,P4) and that the closest pair (which is the P1) has the highest binding energy. We noted that the hydrogen atoms formed a dimer. This is caused by the hydrogen atoms interactions which are responsible for stabilizing the structure. We also observed that the binding trend is weakened with the increases in H-H separation.

We noted that the even pairs have the lowest binding energy which reveals that they are not favourable pairs. For the hydrogenation process, these even pairs are still required but owing to the high amount of adsorption energy this is computationally expensive.

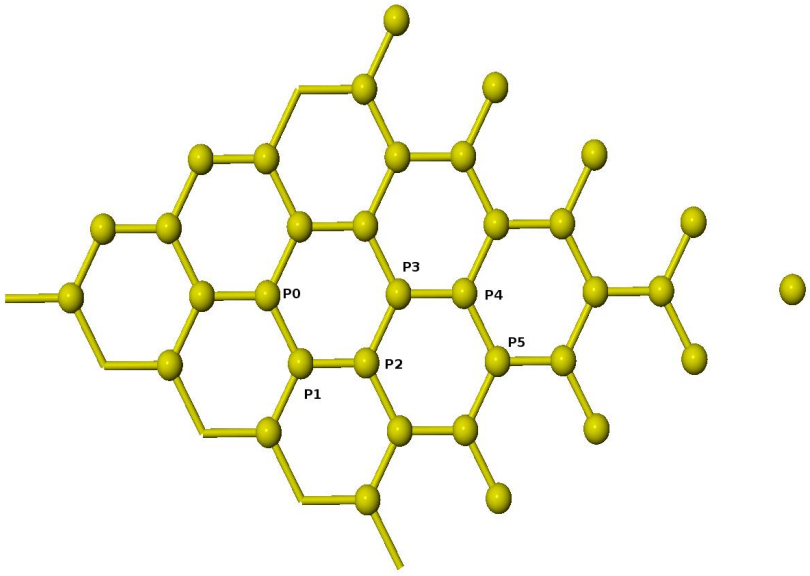

Figure 4.21: Structure of silicon in the graphene structure for a 4x4 supercell. The letter P0 indicates the position where a single hydrogen adatom was adsorbed and is the first hydrogen to be paired with others. P1 to P5 is the route used for pairing with P0.

The geometrical parameters summarized in the table on page 92 are only from pair p1 which was regarded as the most stable pair. Our value for the distance between hydrogen and silicon atoms (H-Si) was not clearly affected by the inclusion of the second hydrogen atom. We observed that when hydrogen atoms are paired, after relaxation they remained symmetric at 1.513$\mathring{A}$. This symmetric position reveals that the hydrogen adatoms clustered are capable of making a planar layer on top of buckled up silicon atoms.

Unlike the situation of carbon in the graphene structure, the (H-Si) bond is longer than the one for single hydrogen adsorption. Our results for the depucking height were seriously affected by the pairing of hydrogen adatoms indicating a value of $0.848\mathring{A}$. This value makes the buckled layer very conspicuous and allows silicon atoms to adopt a structure closer to the one for sp^3 hybridization. The distances between silicon atoms were not seriously affected by the pairing of hydrogen atoms when compared to single adsorption but a slight increment exist. This increase demonstrates that the structural parameters were transformed to be close to the standard one for sp^3 hybridizations.

4.4.2.1 Density of states

We calculated the DOS for hydrogen adatoms adsorbed on the silicon layer. The total DOS for single hydrogen adsorbed on the layer is presented by figure 4.22. We observe a long peak crossing the Fermi level and this is caused by the unpaired electron of carbon. This long peak causes the structure to be metallic. In the valence band, we note a peak of 5 states/eV at the energy of -4eV. This peak is caused by the high contribution of s and p states hybridizations.

The total DOS for a pair of hydrogen adatoms adsorbed on the layer is depicted by figure 4.23. We observe a large band gap of 2.13 eV between the valence and conduction band gap. This band gap indicates that the structure is an insulating, material. Which proves that the adsorption of hydrogen adatoms transforms the structure from sp^2 to sp^3 hybridization and that there are no longer any unpaired electrons. Even in this figure, we still observe the peak at the energy of -4eV in the valence band, but the peak has increased from 5 states/eV to 6 states/eV. This reveals that the second hydrogen adatom increases the number of states by 1 states/eV in the structure. In our calculations, the orbital's contributions is of s and p states, which indicates that

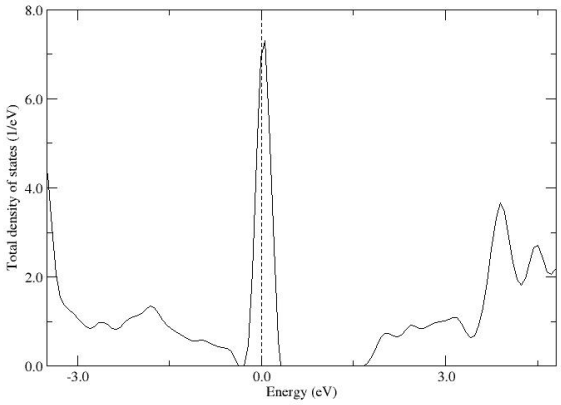

Figure 4.22: The total electronic density of states for a single hydrogen adatom adsorbed on the silicon in the graphene structure.

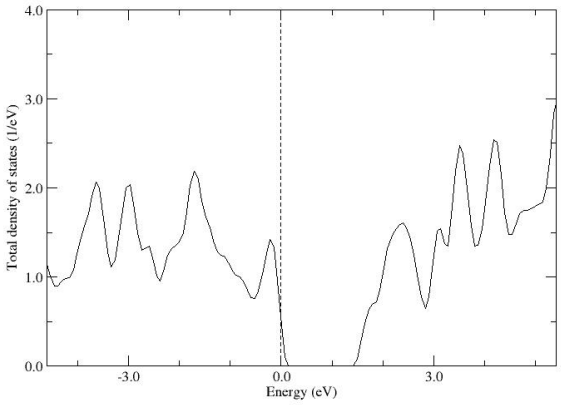

Figure 4.23: The total electronic density of states for a pair of hydrogen adatoms adsorbed on the silicon in the graphene structure.

our calculated band gap is of the s-p type of bonding.

4.4.3 Adsorption of single and pair of hydrogen atoms on SiC atoms in the graphene structure

In this section, the adsorption of hydrogen adatoms on top of SiC atoms in the graphene structure employing four different supercell sizes, i.e. (1x1),(2x2),(3x3) and (4x4), was considered. Firstly, we started by employing the (1x1) unit cell for the adsorption of a hydrogen adatom in order to find the most favourable site between the hollow and the ontop site. Our results reveal that the ontop site is more favourable than the hollow one. The minimum energy for the ontop site was found to be less than the minimum energy for the hollow site by 1.048 eV.

We then considered pairing the hydrogen adatoms at the on top site. Next we determined the most stable configuration between hydrogen adatoms paired at the same side and when they did so on the alternating side. Our calculated binding energy for the same side adsorption was found to be 2.011 eV whereas that for alternating adsorption was found to be 2.835 eV. This binding energy reveals that the alternating adsorption is the favourable configuration. The bond distance between the hydrogen and silicon (H-Si) and hydrogen and carbon (H-C) was found to be 1.536$\mathring{A}$ and 1.133$\mathring{A}$ respectively in the case of same side adsorption whereas on the alternating adsorption the (H-Si) and (H-C) was found to be 1.497$\mathring{A}$ and 1.106$\mathring{A}$ respectively. These results demonstrate that there is stronger bonding on the alternating configuration than on the same side configuration.

The bond distance between carbon and silicon was found to be 1.812$\mathring{A}$ in the same side adsorption whereas on the alternating side the distance was found to be 1.879$\mathring{A}$. This proves that there are stronger transformations from sp^2 to sp^3 hybridization in

the alternating configuration than in the same side configuration. Even in this case, we decided to resume our calculation considering the same side adsorption. Our calculated geometric parameters and binding energies are summarized in the table on page 102.

Table 4.5: The calculated equilibrium height d_{puck} (Å), silicon-carbon [Si-C (Å)] distance and hydrogen-silicon [H-Si (Å)] distance coresponding to different sizes of supercells.

Geometric Parameters		Bond distances		
Single H adatoms	1x1	2x2	3x3	4x4
$d(H-Si)$	1.537	1.523	1.520	1.508
$d(H-C)$	1.125	1.119	1.119	1.116
$d(Si-C)$[H-Si]	1.818	1.843	1.849	1.855
$d(Si-C)$[H-C]	1.894	1.898	1.899	1.898
d_{puck}[H-Si]	0.335	0.379	0.438	0.520
d_{puck}[H-C]	0.625	0.635	0.651	0.706
Pair of H adatoms				
$d(H-Si)$	1.536	1.510	1.508	1.507
$d(H-C)$	1.133	1.127	1.118	1.117
$d(Si-C)$	1.812	1.840	1.843	1.843
d_{puck}[H-Si]	0.299	0.398	0.479	0.634
d_{puck}[H-C]	...	0.582	0.648	0.815
Configurations		Binding energies		
	1x1	2x2	3x3	4x4
P_1	2.011	2.240	2.219	2.294
P_2	....	1.353	1.549	1.482
P_3	...	2.215	2.095	1.987
P_4	...	1.352	1.354	1.352
P_5	...	....	2.090	1.896
Single[H-Si/H-C]	1.022/1.461	1.217/1.489	1.118/1.509	1.319/1.492

The table on page 92 indicates that the growth of the supercells affects our results. In most cases the (4x4) supercell yields better results than the (1x1) unit cell. Starting with the binding energies for single hydrogen adsorption, we observe greater binding energy when hydrogen is on top of carbon than on top of silicon atoms. This reveals that the hydrogen atom prefers to bond with carbon than silicon atoms.

We decided to pair the hydrogen adatoms following the route indicated on figure 4.24. Our results demonstrates that the odd pairs P_1, P_3 and P_5 are the most stable, even if the stability decreased with the greater separation of hydrogen adatoms. Our diagram illustrates that the odd pairs are for hydrogen adsorbed on top of carbon. The even pairs P_2, P_4 and P_6 are for hydrogen adatoms adsorbed on top of silicon atoms and displays less stability. Our results show that the first pair P_1 is the most stable pair.

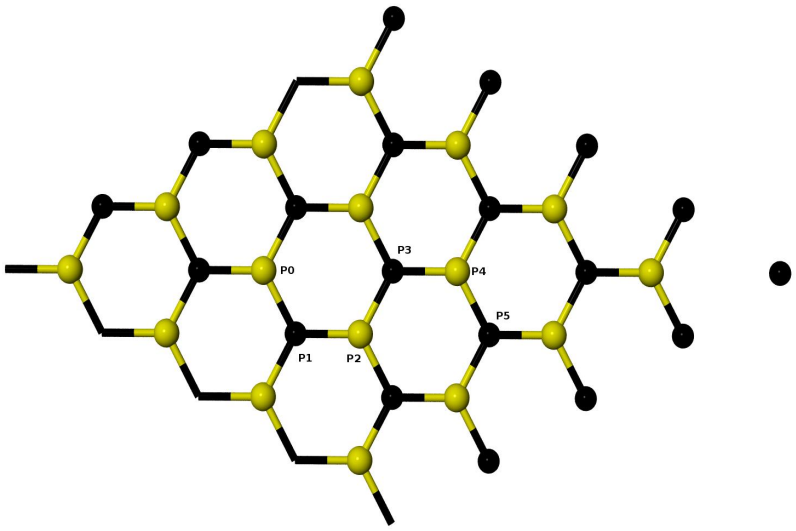

Figure 4.24: Structure of SiC in the graphene structure for a (4x4) supercell. The letter P0 indicates the position where a single hydrogen adatom was adsorbed and is the atom that was employed to pair with others. P1 to P5 is the route used for pairing with P0.

Our presented geometrical parameters are from the P_1 pair. The calculated geometrical parameters show that for single hydrogen adsorption, there is higher bonding between hydrogen and carbon than between hydrogen and silicon atoms. The depucking height for hydrogen adsorption on top of carbon is larger, sometimes twice as large,

than the one for hydrogen adsorbed on top of silicon. This large depucking height reveals the existence of a greater transformation of the structure.

This transformation is also indicated by the silicon-carbon distance of around $1.89\mathring{A}$ in the hydrogen carbon adsorption. This value is almost the same as the one for bulk SiC in the zincblende structure. For the pairing of hydrogen adatoms we note that their depucking heights are not equal. We observe that the SiC layer is buckled and hydrogen adatom remained asymmetric, with the hydrogen adatom on top of silicon being higher than the hydrogen adatom on top of the carbon atom. This is caused by the lesser bonding of hydrogen atoms on top of silicon than on top of carbon. Our results show that the silicon-carbon distance is not really affected by the pairing of hydrogen adatoms. This is caused by the weaker bond of hydrogen with silicon atoms.

4.4.3.1 Density of states

The DOS for single and pair of hydrogen adatoms adsorbed on the SiC layer were calculated in order to find out how the structure is modified. The figures 4.25 and 4.26 present the total DOS for single hydrogen adatoms adsorbed on top of carbon and silicon respectively. The total DOS of paired hydrogen adatoms adsorbed on top of SiC is presented by figure 4.27.

The DOS for single hydrogen adsorbed on top of carbon differs from that for the 2D SiC bulk structure. We observe a high peak crossing the Fermi level which indicates that the structure is metallic. We also see this kind of long peak in the case of a single hydrogen adatom adsorbed on top of silicon atoms. This shows that even in the case of SiC, the hydrogen adatom breaks the double bond between silicon and carbon and leaves a lone pair of electron which is responsible for the metalicity of the structure.

Figure 4.25 depicts a high peak at an energy of around $-6eV$ in the valence band.

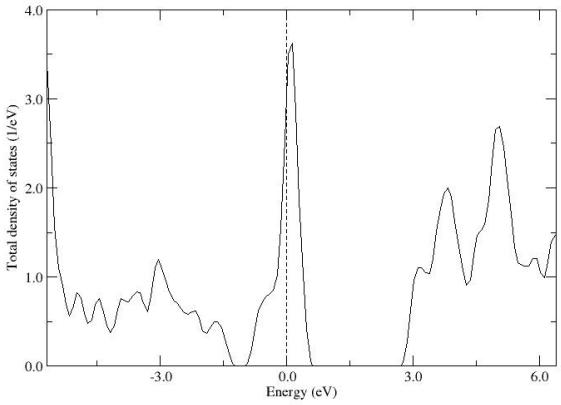

Figure 4.25: The total electronic density of states for single hydrogen adatom adsorbed on top of carbon atom on the SiC in the graphene structure.

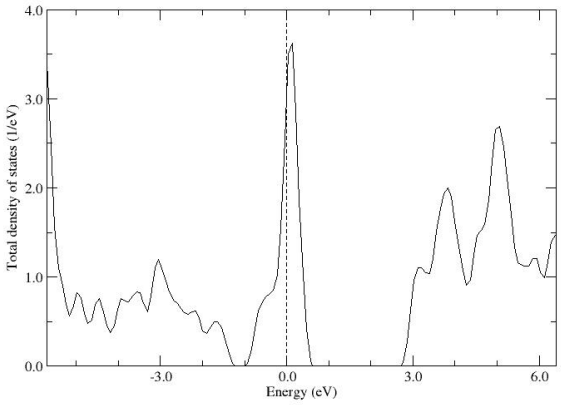

Figure 4.26: The total electronic density of states for single hydrogen adatom adsorbed on top of silicon atom on the SiC in the graphene structure.

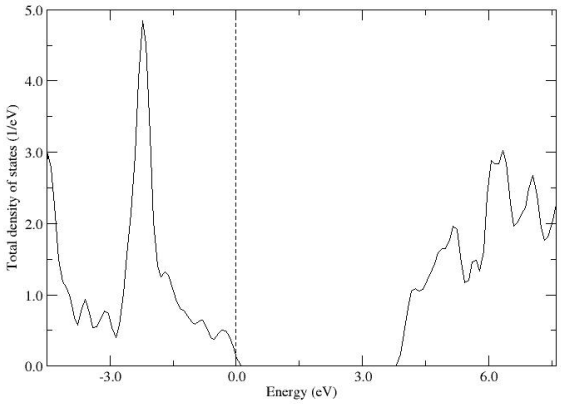

Figure 4.27: The total electronic density of states for paired hydrogen adatoms adsorbed on the SiC in the graphene structure.

This long peak indicates that electrons are energetically excited due to the s and p hybridization. Figure 4.27 illustrates a wide band gap of $3.899eV$ between the valence and the conduction bands. This band gap reveals that the pairing of hydrogen atoms makes the structure to be an insulator. The pairing of hydrogen adatoms in the SiC saturates all the bonds. This band gap is larger than the band gap of pristine SiC in the graphene structure which has a value of $2.542eV$. This indicates that the addition of hydrogen atoms is responsible for fine tuning the band gap. We note a high peak at an energy of $-2eV$ in the valence band which indicates that there is an increase in the number of electrons in the structure during s and p state hybridizations.

Our calculated bond distances between carbon and silicon and depucking heights for the paired hydrogen atoms do not indicate the serious changes when compared to the single hydrogen adsorbed on top of carbon atoms. This reveals that the structural deformation is not responsible for tuning the band gap. This gap is instead tuned by the excess of hydrogen ions H^+ on the structure.

4.4.4 Adsorption of Li adatoms on carbon in the graphene

For adsoption of lithium adatoms, we considered various configurations involving the (1x1), (2x1) and (2x2) two-dimensional unit cells. We considered different coverages involving 25%, 50% upto 100% coverage.

4.4.4.1 Adsorption of Li adatoms employing the (1x1) cell

For 50% coverage, we compare a single Li adatom at the ontop site with the hollow site for a (1x1) cell of graphene. Our results for the fully relaxed systems indicate that the hollow site is lower in energy compared to the ontop site by only $0.046eV$. This is a relatively small energy difference, which shows that under conditions of finite temperature, islands of hollow sites may co-exist with islands of alternate ontop sites. Not surprisingly, these systems are metallic in nature as can be deduced by simple electron counting arguments. The Li-C bond length for the on-top site is 2.19Å and for the hollow site is 1.85Å. The shorter bond length at the hollow site is understandable since the Li ions are freer to approach the graphene plane in this case. For the ontop site attachment, the graphene plane is marginally buckled with the C atom that is attached to the Li atom pushed into the plane by less than 0.05Å. For the hollow site, the graphene sheet remains planar.

Our calculations for 100% coverage on the ontop sites reveal that the Li adatoms attaching on the same side of the graphene sheet possess a lower energy compared with Li adatoms attaching alternately on opposite sides of the graphene sheet. This we find to be a surprising result, since it is different from that of H on graphene. Yang did not report on the case involving Li attaching on the same side of the graphene sheet.

We discovered that one needs to be very careful about the relaxation of the Li adatoms at the ontop sites on the *same* side of the graphene sheet. For our initial

set of calculations, we considered a (1x1) cell. Initially, we placed the two Li adatoms at a distance of 1.80Å directly above the two C atoms. In this case, the Li adatoms relaxed symmetrically to a Li-C bond length of 2.13Å above the graphene sheet. The graphene sheet still remained planar. The energy of this bonded system was *higher* than the sum of the energies of the (1x1) graphene cell and that of two isolated Li atoms by an amount of $3.69eV$. On this basis, it is easy to dismiss the stability of the Li adatoms attaching at the on-top sites on the same side of the graphene layer. For this configuration, the Li-Li bonds are constrained to 1.44Å which should be compared with the nearest-neighbour distance of 3.02Å for Li in the BCC structure. Clearly, this is an energetically unfavoured situation which explains the high energy state of the system. Surprisingly, the atomic relaxation scheme is unable to break this symmetry as the following analysis shows.

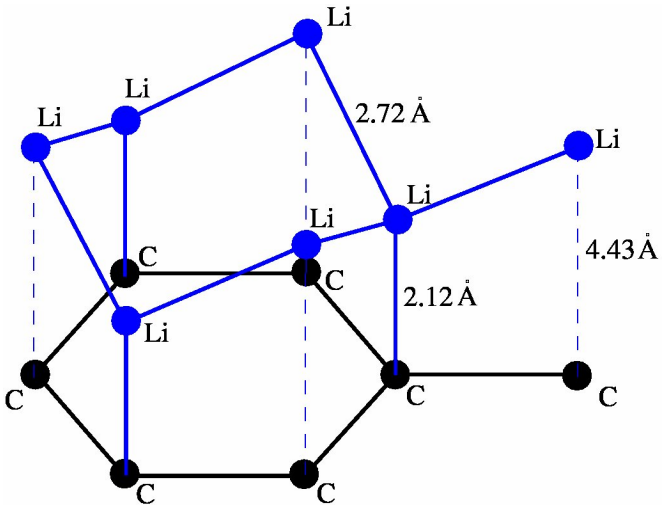

Figure 4.28: The (1x1) cell depicting the two asymmetric on-top site adatoms of Li on the same side of the graphene sheet after relaxation. Not drawn to scale. C=carbon, Li=lithium at the "low" distance of 2.12Å above the C, and at the "high" distance of 4.43Å above the C. The Li-Li bond is 2.72Å.

When we apply a slight staggering to the initial positions of the Li adatoms, a very different scenario results. Here, we placed the Li adatoms asymmetrically at 1.88Å and

1.73Å above the respective C atoms. After relaxation, the Li-C bond lengths relax to 4.43Å ("high") and 2.12Å ("low") respectively. The energy of this bonded system is *lower* than the sum of the energies of the (1x1) graphene cell and of two isolated Li atoms by an amount of $2.58eV$. We refer to this energy difference as the binding energy per (1x1) cell. The odd result is the rather large Li-C bond length of 4.43Å for the "high" Li adatom. We propose that the Li-Li interactions stabilise this arrangement. The shortest Li-Li bondlength is 2.72Å as shown in Figure4.28, which is less than the nearest-neighbour distance of 3.02Å for Li in the BCC structure. An analysis of the charge density distribution shows that the two Li adatoms in the calculational cell are firmly bonded to each other. The "low" Li adatom is strongly bonded to the graphene, but the "high" Li adatom is too far from the graphene sheet to be strongly bonded directly to the graphene sheet. This Li adatom is strongly held in place due to its bonding with its neighbouring Li adatoms. The co-ordination number for the "high" Li adatom is 3, and for the "low" Li adatom is 4.

The energy of this system is *lower* than the sum of the energy of a single Li adatom at the on-top site of the (1x1) graphene sheet and the energy of a single isolated Li atom by an amount of $1.64eV$ which points to the fact that this is a strongly bonded system.

We relaxed the graphene lattice constant for this system comprising the two Li adatoms at the on-top sites on the same side of the (1x1) graphene sheet in the staggered initial configuration. We found that the lattice expands from 2.47Å to 2.56Å, with a relaxation energy of $0.15eV$. The Li-C bond lengths remain essentially unchanged at 4.45Å and 2.12Å respectively.

For Li adatoms attached on alternate sides of the graphene layer, the Li adatoms

relax symmetrically to a Li-C bond length of 2.03Å irrespective of whether the initial positions of the two Li adatoms are symmetric or not. The binding energy per (1x1) cell for this system is $2.36eV$ which is less than that for the case of both the Li adatoms attaching asymmetrically on the same side of the graphene sheet by an amount of $0.22eV$.

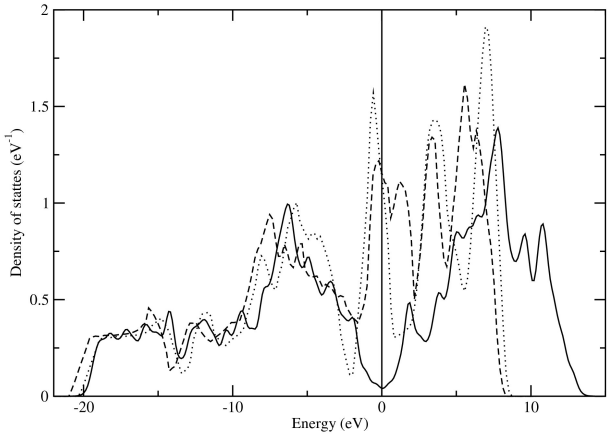

Figure 4.29: The electronic density of states for (i) pure graphene (1x1) (solid), (ii) the two asymmetric on-top site adatoms of Li on the same side of the graphene sheet (dashed), and (iii) the two on-top site adatoms of Li on opposite sides of the graphene sheet (dotted). The Fermi energy is set at $0eV$

Figure4.29 shows the density of electronic states for (i) pure graphene (1x1), (ii) the two asymmetric on-top site adatoms of Li on the same side of the graphene sheet, and (iii) the two on-top site adatoms of Li on opposite sides of the graphene sheet. The figure indicates that there are slight changes to the densities of states for (ii) and (iii) compared to (i) far below the Fermi level, although the overall density of states for (ii) is shifted downwards in energy compared with (i) and (iii). Both (ii) and (iii) show significant changes to the density of states at the Fermi level compared with (i), with (iii) having a greater peak just below the Fermi level. The plot indicates that there are more electrons of high energy (just below the Fermi level) for (iii) compared with (ii).

This gives some justification for the relative stability of (ii) over (iii). We conclude that the bonding is ionic in nature with a net transfer of electronic density from the Li to the graphene substrate.

Our (1x1) unit cell results suggest that we should really view the overlayer not as a mono-layer, but as a bi-layer. Preliminary results for larger system sizes show that the Li overlayer is not smooth with multiple low energy states with varying heights for the Li adatoms. This is easily understood in terms of alternate Li adatoms being pushed out of the plane to accommodate the larger more optimal Li-Li bonding. We do not further consider the 100% coverage of Li at the on-top sites of graphene for the larger calculational cells because this system with its high density of Li adatoms we consider to be difficult to create experimentally. We conclude that it is difficult to force 100% of the Li adatoms onto the on-top sites, which is a meta-stable site. The hollow sites are more stable. At 50% coverage the system prefers the hollow sites.

For coverages beyond 50%, we propose that there will be an admixture of hollow and on-top sites. It is for this reason that we have not considered any further the (1x1) system with 100% coverage at the on-top sites. Caragiu and Finberg [24], in their review of alkali metal absorption on graphite confirm our view that Li on graphene is not properly understood and that the ground state configuration is yet to be confirmed. Our submission, we believe, contributes to the understanding of the plausible structures of Li on graphene for the various different levels of coverages.The hollow site is deemed to be more favourable, and this is what we consider in the next subsection.

4.4.4.2 Adsorption of Li adatoms employing the (2x1) cell

Here we focus on the hollow site, and we expand the calculational cell to a (2x1) cell to increase the number of degrees of freedom for the relaxation of the Li adatoms.

Starting with symmetric initial positions for the Li adatoms at the hollow site set at 1.80Å above the graphene sheet, the system quickly relaxes to a symmetric final state with both adatoms a distance of 1.85Å above the graphene sheet, consistent with the equivalent system for the (1x1) cell.

This we find, however, is not the lowest energy configuration for this system. The (2x1) cell comprising the two Li adatoms attaching on opposite sides of the graphene sheet is lower in energy compared with the two Li adatoms attaching symmetrically on the same side of the graphene sheet by an amount of $0.184eV$ per (2x1) cell. This is still not the lowest energy configuration for this system. When we begin with two Li adatoms attaching on the same side of the graphene sheet, but with slight asymmetries in their initial positions set at 1.88Å and 1.73Å above the graphene sheet, the symmetry is broken and the system is able to find an even lower energy after relaxation.

The (2x1) cell comprising the two Li adatoms attaching asymmetrically on the same side of the graphene sheet is lower in energy compared with the two Li adatoms attaching symmetrically on the same side of the graphene sheet by an amount of $0.73eV$ per (2x1) cell. The asymmetry is stark with one Li adatom pulled toward the graphene layer to a distance of 2.02Å whilst the other being pushed away from the graphene layer to a distance of 3.94Å. The graphene layer remains essentially planar with only slight buckling. To the best of our knowledge, this staggered configuration of Li on graphene has not been investigated before.

A careful analysis of the bond lengths in Figure4.30 shows that this system is once again stabilised by the Li-Li interactions. There are chains of "high" Li adatoms alternating with chains of "low" Li adatoms. This gives rise to a corrugation potential on the surface which warrants further experimental investigation. The Li-Li bond

length across the chains is 3.14Å, which is slightly greater than the nearest neighbour distance in bulk Li. The Li-Li bond length along the chains is 2.49Å which is just the distance between the hollow sites in graphene.

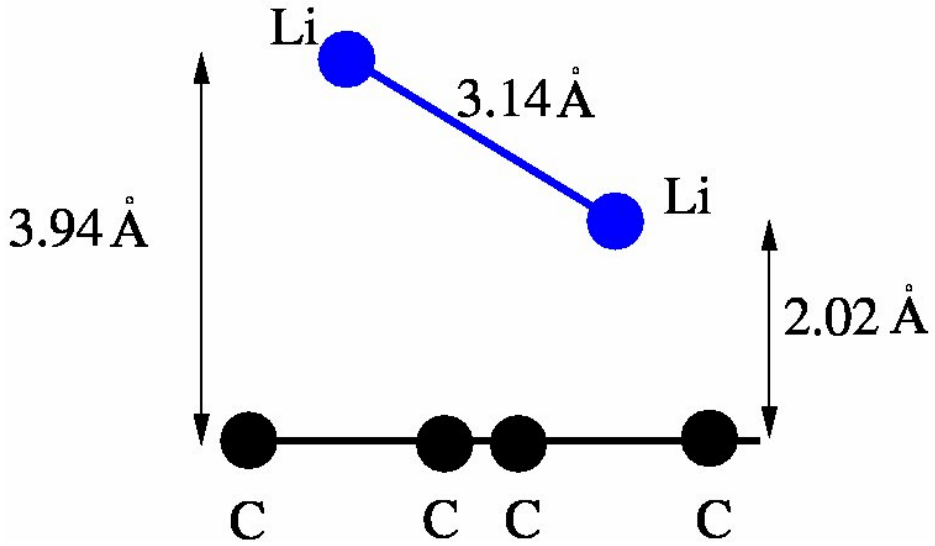

Figure 4.30: The fully relaxed (2x1) cell in front view with the Li adatoms attaching asymmetrically on the same side at the hollow sites. Not drawn to scale. C=carbon, Li=lithium at the "low" distance of 2.02Å above the C, and at the "high" distance of 3.94Å above the C. The Li-Li bond is 3.14Å.

In Figure 4.31 we plot the electronic charge density of this system to investigate the nature of the bonding of this system and the basis for the stability. The diagram indicates that this system is stabilised by the Li-Li interactions along the chains, and there is some distribution of electron density between the staggered Li adatoms. However, the overall density of electrons is low (the iso-surface is set at 0.06eV/Å^3). The bulk of electronic density resides in the graphene layer, which suggests transfer of electronic density from the Li to the graphene resulting in ionic bonding.

We spent a significant effort to investigate the extent to which this is indeed the lowest energy configuration. In particular, we investigated the possible dimerization of the Li adatoms. We considered several initial configurations of the Li adatoms at-

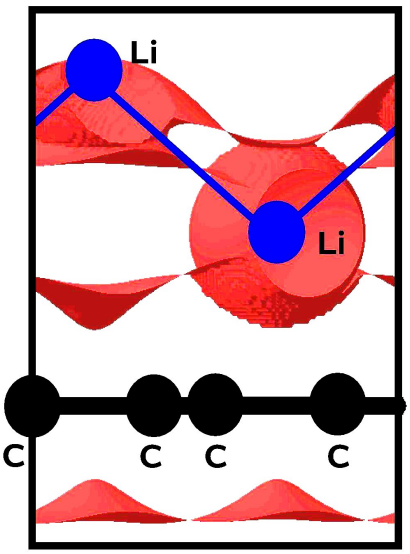

Figure 4.31: The charge density plot for the fully relaxed (2x1) cell with the iso-surface set at 0.06eV/Å^3

taching asymmetrically on the same side of the graphene layer at the hollow sites and with slight xy-displacements of the Li adatoms in the plane of the graphene layer. Our extensive search leads us to conclude that there is no tendency for dimerization, and that the Li adatoms prefer to remain located directly above the hollow sites in the asymmetric final state.

4.4.4.3 Lower coverages of Li adatoms on graphene

We considered 25% coverage of Li adatoms attaching on the same side of the graphene sheet at the hollow sites in the (2x2) cell. This constitutes rows of Li adatoms on the graphene sheet alternating with valleys marked by the absence of Li adatoms. Because of the hexagonal symmetry of the system, there are three degenerate cases all with the same energy. Our fully relaxed calculations for this system show that along the rows the Li adatoms remain centred at the hollow sites. There is no tendency for dimeriza-

tion of the Li adatoms, with the Li-Li bond remaining at 2.46Å which is simply the distance between the hollow sites.

Independent of the initial positions of the Li adatoms (i.e. symmetric or asymmetric initial positions, with or without xy-displacements in the plane of the graphene layer), the final relaxed configuration is symmetric, i.e. not staggered, with the Li adatoms a distance of 1.83Å above the graphene sheet. The binding energy for this system is $2.64eV$ per (2x2) cell. This system has a relatively low density of Li adatoms compared with the previous cases considered above. This enables the Li adatoms to relax readily to a symmetric final configuration.

We also considered an isolated pair of Li adatoms attached on the same side of the graphene sheet at two nearest-neighbour hollow sites. We model this system by constructing a (5x5) cell which is sufficiently large to minimize Li-Li interactions between cells. We considered various initial positions of the Li adatoms, namely symmetric and asymmetric initial positions, with or without xy-displacements in the plane of the graphene layer. Our fully relaxed results show a configuration where the Li adatoms repel each other slightly from a bond length of 2.46Å, which is the distance between the hollow sites, to 2.91Å which may be compared with the Li bond length of 3.02Å in the BCC structure.

The Li adatoms are pushed away slightly from the hollow sites, and are lodged at a distance of 1.85Å above the graphene sheet. There is some buckling of the graphene sheet in the neighbourhood of the Li adatoms. The binding energy of this system is $2.62eV$. This repulsive interaction between the Li adatoms gives credence to our earlier conclusions that the Li adatoms prefer the hollow sites rather than the ontop sites - the latter forces Li-Li interactions over shorter distances (compared with bulk

Li) which is energetically unfavourable. This, of course, has enormous consequences for the electronic structure and the metallic nature of this system.

5

Conclusions

In this work we employed the first principles pseudopotential method within the density functional theory (DFT) and the generalised gradient approximation (GGA, PBE) to perform total energy calculations on bulk and adsorbed systems. We studied various electronic and physical properties of the systems involving carbon, silicon and silicon carbide in the cubic and graphene structures. We utilised the PAW pseudopotential in a methodology based on the plane wave approach. The VASP simulation packages developed at Vienna were used to perform the calculations.

In order to obtain accurate and comparable results to previously published work we initially determined the total energy convergence of carbon and silicon with respect to energy cutoff and k-points sampling of the Brillouin zone. The energy cutoff of carbon was found to be high compared to silicon. The 2p states in carbon are localised because of the lack of a p core state: hence a large number of plane waves is required to achieve a high degree of accuracy.

Once the convergence was successfully tested, we proceeded to calculate the bulk properties of carbon, silicon and silicon carbide in the diamond and graphene struc-

tures. Our results were compared with previous theoretical and experimental results which were available. Interestingly our results within the GGA are very close to the experimental data when compared to the other work where LDA was employed. Since the SiC in the graphene structure is a non-existing experimental structure, our results shows that this structure is plausible and has an interesting properties.

When considering the adsorption of hydrogen adatoms on the graphene structure employing different supercells, we conclude that the 4x4 supercell is suitable for the evaluation of the electronic and physical properties of these systems. The hydrogen adatom prefers to be adsorbed at the ontop site rather than on the hollow site. The binding energies reveal that a pair of hydrogen adatoms prefers to be adsorbed in an alternating manner, one above and one below the graphene plane. But when they are forced to be adsorbed at the same side they form covalent bonds and remain symmetric. This symmetry suggests that hydrogen adatoms prefer to form a planar monolayer ontop of a buckled graphene layer.

But a different scenario occurs when hydrogen adatoms are adsorbed on SiC in the graphene structure. They prefer to be adsorbed on top of a carbon atom rather than ontop of a silicon atom. Our results suggests that we should really view the overlayer of hydrogen adatoms as a bi-layer rather than a monolayer. Our results reveal that the adsorption of hydrogen adatoms must always be paired to avoid the lone pair of carbon electrons which makes the system metallic. When hydrogen adatoms are paired, the bonds are all saturated and the system is transformed into an insulator with a wide range of band gaps. We conclude that the bonding between hydrogen and carbon is covalent. SiC in the graphene structure consists of a wide band gap and the adsorption of hydrogen adatoms increases the band gap even further. We conclude that the hydrogen adatoms may be used to tune the band gap in the semiconductor materials.

When considering Li adatoms on graphene, we conclude that for 100% coverage at the on-top sites, the equilibrium configuration is staggered in nature with alternate Li adatoms pulled in to a distance of 2.12Å("low") and pushed out to a distance of 4.43Å("high") from the graphene plane. The "high" Li adatoms are too far from the graphene sheet to be bonded to the graphene. This system is stabilised by the Li-Li interactions, which is verified by an analysis of the charge density distribution. Our results suggest that we should really view the overlayer not as a mono-layer, but as a bi-layer. For larger system sizes, we note that the Li overlayer is not smooth since it possesses multiple low energy states with varying heights for the Li adatoms. This is understood in terms of alternate Li adatoms being pushed out of the plane to accommodate the larger more optimal Li-Li bonding.

For 50% coverage at the hollow sites, our calculations on the (2x1) cell, which provides more degrees of freedom for relaxation and symmetry-breaking, demonstrate that the lowest energy configuration corresponds to Li adatoms in alternate positions being pulled into and pushed out of the graphene plane in a staggered configuration. There are chains of "high" Li adatoms alternating with chains of "low" Li adatoms. The Li-Li bond length across the chains is $3.14\mathring{A}$, which is slightly greater than the nearest neighbour distance in bulk Li. The Li-Li bond length along the chains is $2.49\mathring{A}$ which is just the distance between the hollow sites in graphene.

The single isolated dimer displays a slight tendency towards repulsion when placed at neighbouring hollow sites. This behaviour helps explain the staggered structure that we observe for the more densely packed surfaces. Our results for the (2x2) cell at 25% coverage at the hollow sites exhibit no staggering as the Li adatoms remain at the hollow sites and relax symmetrically to a distance of $1.83\mathring{A}$ above the graphene sheet.

This constitutes rows of Li adatoms on the graphene sheet alternating with valleys marked by the absence of Li adatoms.

References

[1] http://en.wikipedia.org/wiki/densityfunctionaltheory, 2009-04-06. [34]

[2] http://www.carboncycle.biz/discovery-of-carbon.html, 2010-02-11. [7]

[3] http://www.perkinelmer.com/raman, 2010-01-20. [21]

[4] http://en.wikipedia.org/wiki/Raman_spectroscopy, 2010-01-20. [21]

[5] http://www.abinit.org, 2010-01-15. [55]

[6] http://en.wikipedia.org/wiki/electronicbandstructure, 2010-06-07. [59]

[7] http://www.ioffe.ru/SVA/NSM/semiconductor/diamond, 2009-07-21. [8, 9]

[8] http:doi:10.1016/j.vacuum, 2009.03.018. [10]

[9] http://www.en.wikipedia.org/wiki/Scanning_tunneling_microscope, 2010-01-14. [19]

[10] http://nobelprize.org/nobel-prizes/chemistry/laureates/1998/index.html, 2010-02-26. [33, 56]

[11] http://www.dft.sandia.gov/socorro, 2010-01-15. [55]

[12] A. Andree, M. Le. Lay, T. Zecho, and J. Kuppers. *Chem.Phys.Lett*, 425:99–104, 2006. [25]

[13] A. A. Balandin, S. Ghosh, W. Bao, I. Calizo, D. Teweldebrhan, F. Miao, and C. N. Lau. *Nano.Lett*, 8:902–907, 2008. [17]

[14] A. D. Becke. *Phys.Rev.Lett*, 77:18, 1988. [43]

[15] E. Bekaroglu, M. Topsakal, S. Cahangirov, and S. Ciraci. *Cond-Mat.Mtrl-sci*, ...:1–10, 2010. [ix, 75, 78, 79, 81]

[16] C. Berger, Z. M. Song, T. Li, X. B. Li, A. Y. Ogbanzhi, and R. Feng. *J.Phys.Chem.B*, 108:19912–19916, 2004. [18]

[17] G. Binning and H. Rohrer. *IBM Journal of research and development*, 30:4, 1986. [19]

[18] F. Birch. *Journal of Geophysical Research*, 83:1258–1267, 1978. [65]

[19] P. E. Blochl. *Phys.Rev*, B 50:17953, 1994. [2, 52, 53, 56]

[20] M. Born and J. R. Oppenheimer. *Zur quantentheorie der molekeln*, volume 84. Ann.Physik, 1927. [28]

[21] K. Bradley, J. C. P. Abriel, M. Briman, A. Star, and G. Gruner. *Phys. Rev. Lett*, 91: 218301–218304, 2003. [24]

[22] L. Brewer. *Lawrence Berkeley laboratory report no.LB-3720.* [ix, 69]

[23] G. Calzaferri and R. Rytz. *J.Phys.Chem*, 100:11122–1124, 1996. [70]

[24] M. Caragiu and S. Finberg. *J. Phys. Condens. Matter*, 17:R995, 2005. [106]

[25] S. Casolo, R. Martinanazzo, and G. F. Tantardini. *J.Chem.Phys*, 130:054704, 2008. [24]

[26] D. M. Ceperley and B. J. Alder. *Phys.Rev.Lett*, 45:566, 1980. [41]

[27] K. T. Chan, J. B. Neaton, and M. L. Cohen. *Phys.Rev.B*, 77:235430, 2008. [3, 25]

[28] K. J. Chang and M. L. Cohen. *Phys.Rev B*, 15:8196–8201, 1987. [ix, 65, 67, 68, 69]

[29] J. C. Charlier, X. Blase, and S. Roche. *Carbon*, 79:677, 2007. [7, 10]

[30] Chih-Kai.Yang. *App.phys.Lett*, 94:163115, 1997. [3, 26]

[31] C. D. Clark, P. J. Dean, and P. V. Harris. *Proc.R.Soc.London*, A277:312, 1964. [70]

[32] M. Cohen. *annurev.matsci*, 30:1–26, 2000. [72]

[33] M. L. Cohen. *Phys.Rev*, 1110:293, 1984. [2]

[34] P. A. Denis and F. Iribarne. *THEOCHEM*, 907:93–103, 2009. [ix, 24, 25, 84, 85]

[35] A. R. Denton and N. W. Ashcroft. *Phys.Rev.A*, 43:3161–3164, 1991. [73]

[36] A. Dmitriy, S. Stankovich, E. J. Zimney, R. D. Piner, and G. H. B. Dommett. *Nature*, 448:457–460, 2007. [17]

[37] J. Donohue. *The Structure of Elements*, volume 28. Wiley,New York, 1974. [ix, 69]

[38] D. Elias, R. Nair, T. Mohiuddin, S. Morozov, P. Blake, A. Ferrari, D. Boukhvalov, M. Katsnelson, A. Geim, and K. Novoselov. *Science*, 323:610–613, 2009. [2, 20, 90]

[39] A. Kara et al. *J.Phys.Condens.matter*, 22:045004, 2010. [77]

[40] B. Aufray et al. *J. Appl. Phys*, 45:L837, 2006. [ix, 74, 75, 77]

[41] C. Neto et al. *Rev.Mod.Phys*, 81:109, 2009. [10]

[42] C. Neto et al. *Phys.World*, 105:33, 2006. [10, 12]

[43] E. Stolyarova et al. *PNAS*, 104:9209–9212, 2007. [20]

[44] X. Gonze et al. *Z.Kristallogr*, 220:558–564, 2005. [23]

[45] E. H. L. Falcao, R. G. Blair, J. J. Mack, L. M. Viculis, C. W. Kwon, M. Bendikov, R. B. Kaner, B. S. Dunn, and F. Wudl. *Carbon*, 45:1367, 2007. [18]

[46] A. C. Ferrari, J. C. Meyer, V. Scardaci, C. Casiraghi, and M. Lazzeri. *Phys.Rev.Lett*, 97: 1–4, 2006. [22]

[47] V. Fock. *Z.Phys*, 65:209, 1930. [31, 33]

[48] Arthur. J. Freeman and Erich. Wimmer. *Annual Rev.Mater.Scie*, 25:7–36, 1995. [40]

[49] D. J. Gardiner. *practical Raman spectroscopy*, volume 978. Springer-Verlag, 1989. [21]

[50] A. K. Geim. *Science*, 324:1530, 2009. [10, 11]

[51] L. A. Girifalco and R. A. Lad. *J.Chem.Phys*, 25:693, 1956. [9]

[52] V. P. Guysin, V. A. Miransky, S. G. Sharapov, and I. A. Shovkovy. *Phys.Rev.B*, 102: 195429, 2006. [10]

[53] D. R. Hamann, M. Schluter, and C. Chiang. *Phys.Rev.Lett*, 43:1494, 1979. [2, 52]

[54] B. Hammer, L. B. Hansen, and J. K. Norskov. *Phys.Rev.B*, 59:74:13–21, 1999. [25]

[55] B. Hammer, L. B. Hansen, and J. K. Norskov. *Phys.Rev.B*, 59:7413, 1999. [43]

[56] D. R. Hatree. *The wave mechanics of an atom with non-Coulombic central I, II, III*, volume 24:89,111,426. Proc.Cambridge Phil.Soc, 1928. [30]

[57] L. Hedin and B. I. Lundqvist. *J.Phys.C*, 4:2064, 1971. [42, 67]

[58] W. C. Herring. *Phys.Rev.Lett*, 57:1169, 1940. [46]

[59] P. Hohenberg and W. Kohn. *Phys.Rev*, B864:136, 1964. [34, 36]

[60] L. Hornekaer, Z. Sljivancanin, W. Xu, and R. Otero et al. *Phys.Rev.Lett*, 96:156104, 2006. [25]

[61] W. S. J. R. Hummers and R. E. J. Offeman. *Chem.Soc.*, 80:1339, 1958. [18]

[62] K. Karch, P.Pavone, W.Winl, D.Strauch, and F.Bechstedt. *J.Quantum.Chem*, 56:801–817, 1995. [72, 73]

[63] J. Kerwin and B. Jackson. *J.Chem.Phys*, 128:084702, 2008. [ix, 85]

[64] R. K. Khanna. *Evidence of ion-pairing in the polarized Raman spectra of a Ba2+CrO doped single crystal*, volume 10.1002. John wiley and Sons, Ltd, 1957. [21]

[65] M. Khantha, N. A. Cordero, L. M. Molina, J. A. Alonso, and L. A. Girifalco. *Phys.Rev.B*, 70:125422, 2004. [3]

[66] W. Kohn and L. J. Sham. *Phys.Rev*, 140:A1133, 1965. [43]

[67] W. Kohn and L. J. Sham. *Phys. Rev*, 1133A:140, 1965. [36]

[68] W. Kohn and L. J. Sham. *Phys.Rev*, 561:145, 1966. [36]

[69] G. Kresse and J. Furthmuler. *Phys.Rev.B*, 54:11169, 1996. [55, 56, 58]

[70] G. Kresse and J. Furthmuler. *Comput.Mater.Scie*, 6:15, 1996. [55, 56, 58]

[71] G. Kresse and J. Hafner. *Phys.Rev.B*, 47:558, 1993. [55, 56, 58]

[72] G. Kresse and J. Hafner. *Phys.Rev.B*, 49:14251, 1994. [55, 56, 58]

[73] O. Y. Kwon, S. W. Choi, K. W. Park, and Y. B. Kwon. *Ind.Eng.Chem*, 9:743, 2003. [18]

[74] D. C. Langreth and M. J. Mehl. *Phys.Rev.A*, 38:3098, 1983. [43]

[75] O. Leenaerts, B. Partoens, and F. M. Peeters. *Microelectronics journal*, 40:860–862, 2009. [23, 24]

[76] D. Lueking, H. R. Gutierrez, D. A. Fonseca, D. L. Narayanan, D. V. Essendelft, P. Jain, and C. E. B. Clifford. *J.Am.Chem.Soc*, 128:7758, 2006. [2]

[77] O. Madelung, M. Schulz, and H. Weiss. *Springer-Verlag, Berlin*, 17a:241, 1982. [ix, 69, 72]

[78] R. M. Martin. *Electronic structure:Basic theory and practical methods*, volume 1st edition. Cambridge University Press, 2009. [53]

[79] H. J. Mcskimin and P. Andreatch. volume 43. J.Appl.Phys, 1972. [ix, 69]

[80] J. C. Meyer, C. Kiesielowskie, E. Erni, M. D. Rossell, M. F. Crommie, and A. Zettl. *Nano,Lett*, 8:3582, 2008. [25]

[81] H. J. Monkhorst and J. D. PacK. *Phys.Rev*, B13:5188, 1976. [51, 58, 61]

[82] Z. Ni, Y. Wang, T. Yu, and Z. Shen. *Nano.Rev*, 1:273–291, 2008. [21, 22]

[83] S. Nose. *Mol.Phys*, 52:255–268, 1984. [41]

[84] K. S. Novoselov, A. K. Geim, S. V. Morozov, D. Jiang, Y. Zhang, and et al S. V. Dubonos. *Science*, 306:666–669, 2004. [ix, 10, 18, 23, 74, 75]

[85] K. S. Novoselov, D. Jiang, T. Booth, V. V. Khotkevich, S. M. Morozov, and A. K. Geim. *PNA*, 102:10451, 2005. [10]

[86] K. Oura, V. G. Liefshits, A. A. Saraanin, A. V. Zotov, and M. Katayam. *Surface science*, 98:138–140, 2003. [19]

[87] J. S. Park, A. Reina, R. Saito, J. Kong, G. Dresselhaus, and M. S. Dresselhaus. *Carbon*, 47:1303–1210, 2009. [22]

[88] M. C. Payne, M. P. Tete, D. C. Allan, T. A. Arias, and J. D. Joannopoulos. *Rev.Mod.Phys*, 4:64, 1992. [36, 58]

[89] J. Perdew and A. Zunger. *Phys.Rev.B*, 23:5048, 1981. [42]

[90] J. Perdew, K. Burke, and M. Ernzerhof. *Phys.Rev.Lett*, 77:18, 1996. [43]

[91] J. P. Perdew, K. Burke, and M. Ernzehof. *Phys.Rev.Lett*, 77:3865–3868, 1996. [23]

[92] J. C. Philips and L. Kleiman. *Phys.Rev.B*, 116:287, 1959. [52]

[93] W. Picket. *Comput.Phys.ReV*, 9:115, 1989. [2]

[94] M. A. Pimenta, G. Dresselhaus, M. S. Dresselhaus, L. G. Cancado, A. Jorio, and R. Saito. *Phys.Chem.Chem.Phys*, 9:1276–1291, 2007. [21]

[95] N. R. Ray, A. K. Srivastav, and R. Grotzschel. *In search of graphene-a two dimensional hydrocarbon.* arXiv:0802.3998v1, 2008. [2]

[96] T. Roman, W. A. Dino, H. Nakanisha, H. Kasai, T. Sugimoto, and K. Tange. *Carbon*, 45:203–228, 2007. [ix, 25, 85, 87]

[97] J. Ryou, S. Houng, and G. Kim. *Solid State Communications*, 148:469–471, 2008. [91]

[98] F. Savary, E. Furet, and J. Weder. *J.Molecular Structure:THEOCHEM*, 330:191–195, 1995. [70]

[99] F. Schedin, A. K. Geim, S. V. Morozov, D. Jiang, E. H. Hill, P. Blake, and K. S. Novoselov. *Nat.Mater*, 6:652–655, 2007. [24]

[100] E. Schrodinger. *Phys.Rev*, 28:1049–1070, 2004. [46]

[101] X. Sha and B. Jackson. *Surf.Sci*, 496:318, 2002. [ix, 85]

[102] M. M. Shokrieh and R. Rafiee. *Material.Design*, 31:790–795, 2010. [17]

[103] J. C. Slater. *Phys.Rev*, 34:1293, 1929. [32, 46]

[104] J. O. Sofo, A. S. Chaudhari, and G. D. Barber. *Phys.Rev.B*, 75:153401, 2008. [2]

[105] J. M. Soler, E. Artacho, J. D. Gale, A. Garcia, J. Junquera, P. Ordejon, and D. Sanchez portal. *J.phys.Condens.Matter*, 14:2745, 2002. [24]

[106] M. D. Stoller, S. Park, Y. Zhu, J. An, and R . S. Ruoff. *Nano.Lett*, 8:34983502, 2008. [17]

[107] S. M. Sze. *The physics of semiconductor devices*, volume 83. John Willey and sons (WIE), 2006. [72]

[108] N. Troullier and J. L. Martins. *Phys.Rev B*, 43:1993–2006, 1991. [23]

[109] D. Vanderbilt. *Phys Rev*, B 41:7892, 1990. [2, 52]

[110] L. Vitali, M. Burgahrd, P. Wah, M. A. Schneider, and K. Kern. *Phys.Rev.Lett*, 96:086804, 2006. [20]

[111] D. D. Wagman, W. H. Evans, V. B. Parker, I. Halow, S. M. Baily, and R. H. Schumm. *Natl.Bur.of stand.Tech*, 270-3:96, 1968. [ix, 69]

[112] P. R. Wallace. *Phys.Rev*, 71:622, 1947. [13, 79]

[113] G. Wiech and D.J.Fabian. *In soft x-ray band spectra and the electronic structure of metals and materials*, volume 32. Academic press,London,New york, 1968. [73]

[114] Z. Wu and R. E Cohen. *Phys.Rev.B*, 73:235116, 2006. [44]

[115] D. H. Yeah and J. R. Riter. *J. Phys.Chem.Solids*, 32:653, 1971. [ix, 69]

[116] M. T. Yin and M. L. Cohen. *Phys.Rev.B*, 24:6121–6124, 1981. [67, 68]

[117] M. T. Yin and M. L. Cohen. *Phys.Rev.Lett*, 45:1004, 1980. [ix, 69]

[118] R. D. Young. *Rev.Scie.Instrument*, 37:275, 1966. [19]

[119] Y. Zhang and W. Yang. *Phys.Rev.Lett*, 80:890, 1998. [43]